Engineering Structures 173 (2018) 283–299

Contents lists available at ScienceDirect

Engineering Structures

journal homepage: www.elsevier.com/locate/engstruct

Co-rotational 3D beam element for nonlinear dynamic analysis of risers manufactured with functionally graded materials (FGMs)

J.C.R. Albino[a,*], C.A. Almeida[b], I.F.M. Menezes[b], G.H. Paulino[c]

[a] Department of Mechanical Engineering, SENAI CIMATEC, BA 41650-010, Brazil
[b] Department of Mechanical Engineering, Pontifical Catholic University of Rio de Janeiro, RJ 22453-900, Brazil
[c] School of Civil and Environmental Engineering, Georgia Institute of Technology, Atlanta, GA 30332, USA

ARTICLE INFO

Keywords:
Co-rotational formulation
3D beam element
Nonlinear analysis
Functionally graded materials
Marine risers

ABSTRACT

This paper considers a co-rotational beam formulation for beams, which is used for the finite element analysis of flexible risers and pipelines made of functionally graded materials. The influence of material gradation is addressed using an exponential variation of properties throughout the thickness of the pipe. Space discretization of the equilibrium equations is derived based on the Euler–Bernoulli assumptions considering two-node Hermitian beam elements which are referred to a co-rotation coordinate system attached to the element local frame of coordinates. The geometric non-linear effects of the beam are considered under large displacement and rotations, but under small-strain conditions. The deflections of the riser result from forces caused by self-weight, buoyancy, sea currents, waves, the action of floaters, seabed-structure interactions, and ship's motion. We provide numerical examples and compare our results with the ones available in the literature. In addition, applications related to practical offshore engineering situations are considered to highlight the behavior of functionally graded materials (FGMs) as compared to homogeneous risers.

1. Introduction

Flexible marine risers are used to transport oil from a wellhead on the seabed to platforms based on floating production systems, such as Spar, Floating Production Storage and Offloading (FPSO), semi-submersibles and Tension-Leg Platform (TLP). A marine riser is continuously subjected to severe environmental loading from currents, waves, and winds. For this reason, marine risers are considered one of the most critical parts of a complex offshore production system. Their failure can severely deteriorate the marine environment and interrupt the oil production, causing costly environmental recovery and lost production.

Owing to their low flexural rigidity, as compared to their axial rigidity, marine risers undergo large changes in curvature under operating loads. As a result, one needs to consider geometric nonlinearities for their structural evaluation. In some special circumstances in which marine piping undergoes (a) large deformations and (b) negligible tensile loading, its bending stiffness may become insignificant as compared to other local effects, such as cross-section ovalization [1]. In these special cases, the analysis of marine piping requires a more detailed numerical model [2,3].

Computational models based on the finite element method for static and dynamic analysis of risers involving geometric nonlinearity have been the subject of extensive research [4–12]. These models employ the classical theory of beams under finite rotations and the governing equilibrium equations are obtained from the following three basic descriptions: total lagrangian, updated lagrangian and co-rotational. The first two approaches use, respectively, the undeformed and deformed configurations, as a reference for both static and kinematic variables. Both total and updated Lagrangian formulations have been extensively used in the literature in various beam element formulations [13–17] and the only advantage of using one over the other lies in their numerical efficiency. However, under significantly large rotations, these two formulations may cause spurious stiff solutions because of the non-vectorial nature of rotation variables. To overcome such a difficulty, co-rotational formulations have been proposed in the literature [18–21] as a framework for nonlinear analysis of one-dimensional finite element models such as beam elements. In this approach, the total motion of a beam is decomposed into two parts: rigid body and pure deformational. The deformation is measured from a rotating frame attached to the element undeformed configuration, and standard linear formulation solutions are employed in the numeric incremental procedure in such a way that non-linearity is considered by the spatial rotation of the undeformed reference frame. This procedure is particularly well fitted for the finite element representation of slender pipe kinematics, such as in

* Corresponding author.
E-mail addresses: jc.romeroal@outlook.com (J.C.R. Albino), calmeida@puc-rio.br (C.A. Almeida), ivan@puc-rio.br (I.F.M. Menezes), paulino@gatech.edu (G.H. Paulino).

https://doi.org/10.1016/j.engstruct.2018.05.092
Received 10 October 2017; Received in revised form 21 May 2018; Accepted 24 May 2018
Available online 05 July 2018

marine riser structures undergoing large three-dimensional displacements. This study considers axial, bending, and torsional deformations, but neglects transverse cross-section deformations of the pipe.

Oil exploration has shifted into more remote locations and ultra-deep water under severe operating conditions, demanding lightweight, strong, durable riser structures to reduce production costs and increase efficiency. In this regard, the use of composite materials for risers [22,23] is quite promising because, as compared to traditional materials, they offer a high stiffness to weight ratio, high tensile and fatigue strength, improved structural damping, low thermal conductivity, and good corrosion resistance. However, delamination is a critical damage mechanism in traditional composite materials under extreme mechanical and thermal loadings [24]. As a solution to this problem, material scientists from Japan proposed in the mid 1980s the concept of functionally graded materials (FGMs) [25] to design a thermal barrier capable of withstanding a temperature gradient of 1000 K across a 10-mm cross-section. These materials provide continuous graded macroscopic properties with gradual change in microstructure and are designed to take advantage of the desirable features of their constituents phases. Due to the material gradation, FGMs have no material interfaces, thus eliminating the possibility of delamination, as it is the case in traditional composite materials.

Over the last years, FGMs have been used in different industrial fields such as aerospace, nuclear science, defense, automotive and energy conversion. For instance, functionally graded (FG) plates as well as FG cylindrical shells have been reported in the literature on bending, vibration and buckling analysis [26–34].

An ideal material for marine risers would combine the best properties of metals at inner surfaces, such as toughness and machinability, and of ceramics at outer surfaces, such as high strength and temperature resistance. This would be a very effective engineering solution but requires material usage to an extent not feasible for production in our days. However, FGMs could be employed as a transition material in multi-layer riser cross-sections to prevent abrupt differences in mechanical and thermal properties and avoid debonding at certain extreme loading conditions. Because cracks are likely to initiate at interfaces and propagate into the weaker material sections, FGMs can reduce the effects of thermal, residual, or stress concentration factors [17]. Although still not available in full-scale industrial production, FGMs are man-made materials in which the method of fabrication, geometry, reinforcement location, and matrix alloy may be tailored to achieve certain desired properties.

In this study, we present a concept for marine risers that considers material gradation throughout the pipe thickness. The FGM model is isotropic with constant Poisson's ratio and its non-homogeneity arises from the variation of the Young's modulus (E) and the density (ρ) in the thickness direction according to a power law [31,35]. A beam element model based on Euler-Bernoulli kinematics is adopted, which considers both geometric nonlinearities and a mass matrix derived in closed form. In the next two sections, details of a 3D co-rotational beam finite-element formulation are given with constitutive relations associated to FGM capabilities incorporated. The formulation was implemented, and in Section 4 the results of some sample analyses are presented that illustrate the important features of graded material usage in marine risers and the effect of its non-homogeneity on the stress distribution.

2. Description of the 3D co-rotational beam model

This section presents details of the 3D co-rotational beam formulation used in the present study.

2.1. Basic assumptions

The following hypotheses are adopted to derive the behavior of the beam element:

- plane sections remain plane and perpendicular to the beam centerline after deformation (Euler-Bernoulli hypothesis);
- large displacements are allowed but only under small strain conditions;
- the material behaves elastically, and thus, element model nonlinearities result from both the spatial configuration at each instant of the analysis and the coupling of axial tension and bending deformation mechanisms; and
- under torsion loadings, the cross-section remains plane, i.e., it does not warp.

2.2. Coordinate systems

A co-rotational beam element undergoing large displacements and rotations is shown in Fig. 1. In this figure, we identify three configurations: initial configuration ($\mathscr{C}_0$), which is the element in its initial (undeformed) position at time t = 0; co-rotated configuration ($\mathscr{C}_C$), which is the element after it has been subjected to rigid body movements from its initial configuration; and deformed configuration ($\mathscr{C}_D$), which is the element in its current configuration at time t under external loading. Coordinate systems attached to the beam element at each configuration are also shown in Fig. 1 and are described as follows:

- the global frame (X_G, Y_G, Z_G) is a coordinate system describing the structure, and this system remains fixed during the entire analysis;
- the element base frame (X_0, Y_0, Z_0) is the coordinate system of the element at its initial configuration ($\mathscr{C}_0$); in this configuration, the beam element is assumed to be straight and the X_0-axis coincides with the element longitudinal direction; the other axes (Y_0 and Z_0) are set to the cross-section principal directions;
- the co-rotated frame (X_C, Y_C, Z_C) is associated with the co-rotated configuration ($\mathscr{C}_C$); the X_C-axis passes through two end nodes of the element; on this system, the entire element formulation is written; and
- the convective frame (X_D, Y_D, Z_D) is associated with the deformed configuration ($\mathscr{C}_D$); this system follows the element centerline in the deformed configuration and is attached to its center; the X_D-axis defines the cross-section orientation, and the other axes (Y_D and Z_D) are chosen along the cross-sectional principal directions.

2.3. Local beam kinematics

In this section, compatibility relations for a 3D beam model used to represent the structural behavior of risers are derived. Fig. 2 presents successive positions at two instants of analyses separated by a time increment Δt. A general point P in the riser moves from points P^t to $P^{t+\Delta t}$

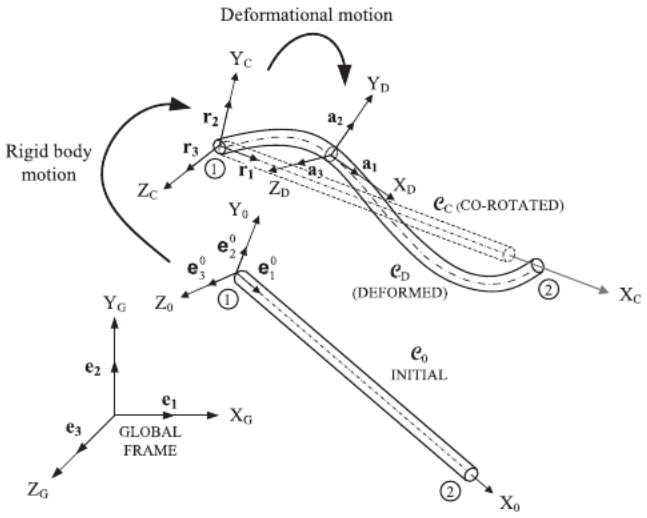

Fig. 1. Co-rotational frame of a deformed beam element.

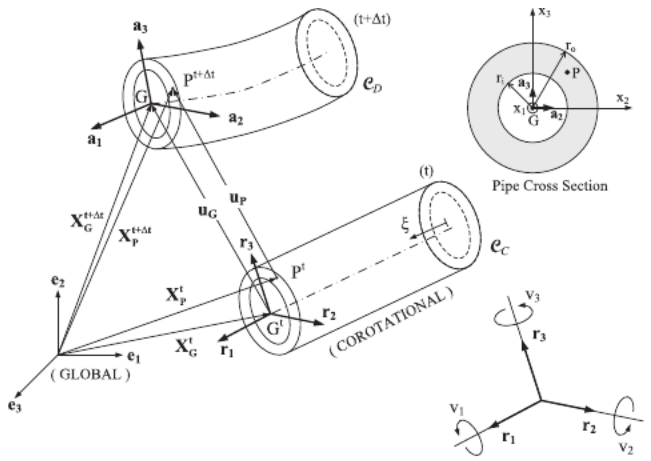

Fig. 2. Beam kinematics and coordinate systems.

with a displacement increment vector $\mathbf{u}_P = {}^{t+\Delta t}_{P} - {}^{t}_{P}$ obtained from position vector differences defined in the global coordinate system

$${}^{t}_{P} = {}^{t}_{G} + x_2\,{}_2 + x_3\,{}_3 \qquad {}^{t+\Delta t}_{P} = {}^{t+\Delta t}_{G} + x_2\,{}_2 + x_3\,{}_3 \tag{1}$$

where ${}^{t}_{G}$ and ${}^{t+\Delta t}_{G}$ are cross-section centerline position vectors in co-rotated and deformed configurations, respectively, and the two pairs of unit vectors ${}_2$ and ${}_3$ and, $\mathbf{r}_2$ and $\mathbf{r}_3$ are axes of principal directions of inertia attached to the cross-section of the beam in both configurations.

Considering the element cross-section, local coordinates x_2 and x_3 should satisfy the geometric condition $r_i \leqslant (x_2^2 + x_3^2)^{1/2} \leqslant r_o$, where r_i and r_o are, respectively, cross-sectional internal and external radii. Orthogonal vector bases $\mathbf{r}_i$ and ${}_i$ (i = 1, 2, 3), are related by a transformation (rotation) matrix

$${}_i = \quad {}_i \quad (i = 1, 2, 3) \tag{2}$$

In large displacement analyses, the cross-section rotations of risers are no longer small enough to be treated as rotational vectors because the obtained finite measures do not satisfy classical linear algebra rules such as the commutative vector property [36]. Thus, a pseudovector rotation is conveniently defined as

$$= v_1\,{}_1 + v_2\,{}_2 + v_3\,{}_3 = \quad \psi \tag{3}$$

where v_i $(i = 1, 2, 3)$ are cross-section rotation increments at time interval Δt referred to vector base $\mathbf{r}_i$. This definition stems from a geometric property that any finite rotation can be properly represented by a single rotation of an angle

$$\psi = \sqrt{v_1^2 + v_2^2 + v_3^2} \tag{4}$$

about the spatial axis parallel to the unit vector $\mathbf{e}$.

The orthogonal rotation matrix in Eq. (2), written in terms of $\boldsymbol{\Psi}$, has the following representation

$$= + \frac{\sin\psi}{\psi}\,(\ ) + \frac{1}{2}\left(\frac{\sin(\psi/2)}{\psi/2}\right)^2 (\ )\,(\ ) \tag{5}$$

where $\mathbf{I}$ is the identity matrix (third order) and $(\ )$ is a skewed symmetric matrix defined by

$$(\ ) = \begin{bmatrix} 0 & -v_3 & v_2 \\ v_3 & 0 & -v_1 \\ -v_2 & v_1 & 0 \end{bmatrix} \tag{6}$$

Applying Taylor series expansion to the trigonometric functions in Eq. (5) and retaining all terms up to the second order, an approximate expression for the transformation matrix gives

$$= + (\ ) + \frac{1}{2}\,(\ )\,(\boldsymbol{\Psi}) \tag{7}$$

By substituting Eq. (6) into Eq. (7), we obtain

$$= \begin{bmatrix} 1-\frac{v_2^2+v_3^2}{2} & -v_3 + \frac{v_1 v_2}{2} & v_2 + \frac{v_1 v_3}{2} \\ v_3 + \frac{v_1 v_2}{2} & 1-\frac{v_1^2+v_3^2}{2} & -v_1 + \frac{v_2 v_3}{2} \\ -v_2 + \frac{v_1 v_3}{2} & v_1 + \frac{v_2 v_3}{2} & 1-\frac{v_1^2+v_2^2}{2} \end{bmatrix} \tag{8}$$

which substituted into Eq. (2) and the obtained expressions for ${}_i$ into Eq. (1), results in the following components of displacement increment vector components

$$\begin{aligned} u_{P_1} &= u_1 - x_2 v_3 + x_3 v_2 \quad + \frac{1}{2}x_2 v_1 v_2 + \frac{1}{2}x_3 v_1 v_3 \\ u_{P_2} &= u_2 \quad - x_3 v_1 \quad -\frac{1}{2}x_2\left(v_1^2 + v_3^2\right) + \frac{1}{2}x_3 v_2 v_3 \\ u_{P_3} &= \underbrace{u_3 + x_2 v_1}_{\text{Linear}} \quad \underbrace{+\frac{1}{2}x_2 v_2 v_3 - \frac{1}{2}x_3\left(v_1^2 + v_2^2\right)}_{\text{Non-Linear}} \end{aligned} \tag{9}$$

where u_1, u_2, and u_3 are the cross-section centerline displacement increments, components of vector $\mathbf{u}_G = {}^{t+\Delta t}_{G} - {}^{t}_{G}$, in Fig. 2.

The Green-Lagrange deformation components contributing to the deformation energy in the principle of virtual work (PVW), are expressed, with respect to the local reference axes $\mathbf{r}_i$ [13], in terms of the displacement of a point P in the form

$$\begin{aligned} \varepsilon_{11} &= u_{P_{1,1}} + \tfrac{1}{2}(u_{P_{1,1}})^2 + \tfrac{1}{2}(u_{P_{2,1}})^2 + \tfrac{1}{2}(u_{P_{3,1}})^2 \\ \gamma_{12} &= u_{P_{1,2}} + u_{P_{2,1}} + u_{P_{1,1}}u_{P_{1,2}} + u_{P_{2,1}}u_{P_{2,2}} + u_{P_{3,1}}u_{P_{3,2}} \\ \gamma_{13} &= u_{P_{1,3}} + u_{P_{3,1}} + u_{P_{1,1}}u_{P_{1,3}} + u_{P_{2,1}}u_{P_{2,3}} + u_{P_{3,1}}u_{P_{3,3}} \end{aligned} \tag{10}$$

In Eqs. (10), a comma after an index means differentiation of a displacement increment component with respect to the coordinate. Displacement increment measures in Eqs. (10) are expressed up to a second-order approximation. The incremental numerical procedure allows us to follow the exact solution if sufficiently small load increments are used.

Substituting Eq. (9) into Eq. (10) and eliminating the algebraic

$$\begin{aligned} \varepsilon_{11} &= u_{1,1} - x_2 v_{3,1} + x_3 v_{2,1} \quad + \frac{1}{2}\left(u_{2,1}^2 + u_{3,1}^2\right) + x_2\left[\frac{1}{2}\left(v_{1,1}v_2 + v_1 v_{2,1}\right) + u_{3,1}v_{1,1}\right] \\ &\quad + x_3\left[\frac{1}{2}\left(v_{1,1}v_3 + v_1 v_{3,1}\right) - u_{2,1}v_{1,1}\right] + \frac{1}{2}\left(x_2^2 + x_3^2\right)v_{1,1}^2 \\ &\quad + \frac{1}{2}\left(x_2^2 v_{3,1}^2 + x_3^2 v_{2,1}^2\right) - \left(x_2 x_3\right)v_{3,1}v_{2,1} \\ \gamma_{12} &= u_{2,1} - v_3 - x_3 v_{1,1} \quad + \frac{1}{2}v_1 v_2 + u_{3,1}v_1 - \frac{1}{2}x_3\left(v_{2,1}v_3 - v_2 v_{3,1}\right) \\ \gamma_{13} &= \underbrace{u_{3,1} + v_2 + x_2 v_{1,1}}_{\text{Linear}\,(e_{ij})} \quad \underbrace{+\frac{1}{2}v_1 v_3 - u_{2,1}v_1 + \frac{1}{2}x_2\left(v_{2,1}v_3 - v_2 v_{3,1}\right)}_{\text{Non-Linear}(\eta_{ij})} \end{aligned}$$

terms of order higher than two, deformation increments in terms of the displacement increments of a cross-section results in the following equations
which are geometrically compatible with deformation kinematics.

3. Incremental equilibrium equations for highly deformed FGM risers

3.1. Co-rotational updated Lagrangian formulation

The element formulation is obtained considering the linear (e_{ij}) and nonlinear (η_{ij}) strain contributions in the imposition of the PVW. Thus, considering the equilibrium of the structure at time t+ Δt, with respect to the latest co-rotated configuration at time t, the PVW for the updated Lagrangian formulation gives

$$\int_{{}^{t}V} {}^{t+\Delta t}_{t}S_{ij}\,\delta\,{}^{t+\Delta t}_{t}\varepsilon_{ij}\,d\,{}^{t}V = {}^{t+\Delta t} \tag{12}$$

where ${}^{t+\Delta t}$ is the external virtual work due to surface and body forces

$${}^{t+\Delta t} = \int_{{}^{0}S} {}^{t+\Delta t}_{0}f_i^{S}\,\delta u_i\,{}^{S}d\,{}^{0}S + \int_{{}^{0}V} {}^{t+\Delta t}_{0}f_i^{B}\,\delta u_i\,d\,{}^{0}V \tag{13}$$

In Eqs. (12) and (13), δu_k is the virtual variation in the displacement components ${}^{t+\Delta t}u_k$, and ${}^{t+\Delta t}_{t}S_{ij}$ and ${}^{t+\Delta t}_{t}\varepsilon_{ij}$ are the components of the second Piola-Kirchhoff stress and the Green-Lagrange strain tensors, respectively. These two tensors correspond to the configuration at time (t+Δt) but measured in the reference frame at time t.

To develop a linearized incremental solution [13] for the nonlinear Eq. (12), the following decompositions are used

$${}^{t+\Delta t}_{t}S_{ij} = {}^{t}\tau_{ij} + \Delta\tau_{ij}, \qquad {}^{t+\Delta t}_{t}\varepsilon_{ij} = {}^{t}\varepsilon_{ij} + \Delta\varepsilon_{ij} \tag{14}$$

where ${}^{t}\tau_{ij}$ are the Cauchy stress tensor components at time t and $\Delta\tau_{ij}$ and $\Delta\varepsilon_{ij}$ are the stress and strain tensors increments. As shown in Eq. (11), the strain increment components are decomposed in linear (Δe_{ij}) and nonlinear ($\Delta\eta_{ij}$) as

$$\Delta\varepsilon_{ij} = \Delta e_{ij} + \Delta\eta_{ij} \tag{15}$$

From the above discussions, Eq. (12) can be written as

$$\int_{{}^{t}V} ({}^{t}\tau_{ij} + \Delta\tau_{ij})\,\delta\,({}^{t}\varepsilon_{ij} + \Delta e_{ij} + \Delta\eta_{ij})\,d\,{}^{t}V = {}^{t+\Delta t} \tag{16}$$

where $\delta\,{}^{t}\varepsilon_{ij} = 0$ (because the element is subjected to rigid body motions only in the reference configuration), and assuming a linear elastic approximation for the incremental stresses and strains $\Delta\tau_{ij} = {}_{t}C_{ijrs}\,\Delta e_{rs}$, one obtains:

$$\int_{{}^{t}V} {}_{t}C_{ijrs}\Delta e_{rs}\,\delta\Delta e_{ij}\,d\,{}^{t}V + \int_{{}^{t}V} {}^{t}\tau_{ij}\,\delta\Delta\eta_{ij}\,d\,{}^{t}V = {}^{t+\Delta t} - \int_{{}^{t}V} {}^{t}\tau_{ij}\,\delta\Delta e_{ij}\,d\,{}^{t}V \tag{17}$$

In this equation, the left-hand side leads to the linear and nonlinear stiffness matrices, and the right-hand side leads to the external and internal force vectors. Eq. (17) was employed in the static analysis.

In the formulation of dynamic problems, including the beam inertia, the PVW was generalized by the D'Alembert's principle [37]. Then, using Newton's second law and the term corresponding to the body forces in Eqs. (12) and (13), one obtains

$$\int_{{}^{t}V} {}^{t+\Delta t}_{t}S_{ij}\,\delta\,{}^{t+\Delta t}_{t}\varepsilon_{ij}\,d\,{}^{t}V = \int_{{}^{0}S} {}^{t+\Delta t}_{0}f_i^{S}\,\delta u_i\,{}^{S}d\,{}^{0}S + \int_{{}^{0}V} ({}^{t+\Delta t}_{0}f_i^{B} - {}^{0}\rho\,{}^{t+\Delta t}\ddot{u}_i)\,\delta u_i\,d\,{}^{0}V \tag{18}$$

By adding the term corresponding to the viscous damping in Eq. (18), we obtain the incremental equation of dynamic equilibrium

$$\begin{aligned}\int_{{}^{0}V} {}^{0}\rho\,{}^{t+\Delta t}\ddot{u}_i\,\delta u_i\,d\,{}^{0}V + \int_{{}^{0}V} k\,{}^{t+\Delta t}\dot{u}_i\,\delta u_i\,d\,{}^{0}V + \int_{{}^{t}V} {}_{t}C_{ijrs}\,\Delta e_{rs}\,\delta\Delta e_{ij}\,d\,{}^{t}V \\ + \int_{{}^{t}V} {}^{t}\tau_{ij}\,\delta\Delta\eta_{ij}\,d\,{}^{t}V = \int_{{}^{0}S} {}^{t+\Delta t}_{0}f_i^{S}\,\delta u_i^{S}\,d\,{}^{0}S + \int_{{}^{0}V} {}^{t+\Delta t}_{0}f_i^{B}\,\delta u_i\,d\,{}^{0}V \\ - \int_{{}^{t}V} {}^{t}\tau_{ij}\,\delta\Delta e_{ij}\,d\,{}^{t}V\end{aligned} \tag{19}$$

In the next section, equilibrium Eq. (19) will be written in its matrix form considering the structure displacements discretization by using interpolation functions.

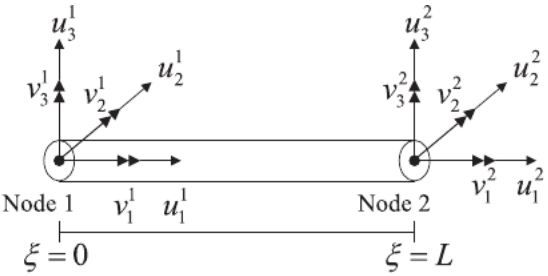

Fig. 3. 3D beam element.

3.2. Derivation of interpolation matrix and global dynamic equilibrium equation

For the finite element solution of Eq. (19), a two-node beam model was considered under Euler-Bernoulli assumptions with active axial, bending, and torsion displacements, all interpolated along its length L using a one-dimensional Hermite polynomial - ξ coordinate along the element as shown in Fig. 3. Thus, the incremental displacement field of the cross-section center line within the element results in

$$\begin{aligned}u_1(\xi) &= \phi_1(\xi)u_1^1 + \phi_2(\xi)u_1^2 \\ u_2(\xi) &= \phi_3(\xi)u_2^1 + \phi_4(\xi)u_2^2 + \phi_5(\xi)v_3^1 - \phi_6(\xi)v_3^2 \\ u_3(\xi) &= \phi_3(\xi)u_3^1 + \phi_4(\xi)u_3^2 - \phi_5(\xi)v_2^1 + \phi_6(\xi)v_2^2 \\ v_1(\xi) &= \phi_1(\xi)v_1^1 + \phi_2(\xi)v_1^2 \\ v_2(\xi) &= -\phi_7(\xi)u_3^1 + \phi_7(\xi)u_3^2 + \phi_8(\xi)v_2^1 - \phi_9(\xi)v_2^2 \\ v_3(\xi) &= \phi_7(\xi)u_2^1 - \phi_7(\xi)u_2^2 + \phi_8(\xi)v_3^1 - \phi_9(\xi)v_3^2\end{aligned} \tag{20}$$

where ϕ_i are the finite element shape functions for beams, as defined in Appendix B.1.

The linear terms in Eq. (9) relative to the displacements at any point P in the pipe cross-section are expressed as

$$\begin{aligned}u_{P_1}(\xi, x_2, x_3) &= u_1 - x_2 v_3 + x_3 v_2 \\ u_{P_2}(\xi, x_2, x_3) &= u_2 - x_3 v_1 \\ u_{P_3}(\xi, x_2, x_3) &= u_3 + x_2 v_1\end{aligned} \tag{21}$$

The displacement fields in Eq. (21) can be written in a matrix form after replacing Eq. (20) in (21), and one obtains

$$\mathbf{u} = [u_{P_1} \;\; u_{P_2} \;\; u_{P_3}]^T = (\xi, x_2, x_3)\mathbf{u} \tag{22}$$

where (ξ, x_2, x_3) is the element interpolation matrix defined as

$$= \begin{bmatrix} \phi_1 & -x_2\phi_7 & -x_3\phi_7 & 0 & x_3\phi_8 & -x_2\phi_8 & \phi_2 & x_2\phi_7 & x_3\phi_7 & 0 & -x_3\phi_9 & x_2\phi_9 \\ 0 & \phi_3 & 0 & -x_3\phi_1 & 0 & \phi_5 & 0 & \phi_4 & 0 & -x_3\phi_2 & 0 & -\phi_6 \\ 0 & 0 & \phi_3 & x_2\phi_1 & -\phi_5 & 0 & 0 & 0 & \phi_4 & x_2\phi_2 & \phi_6 & 0 \end{bmatrix} \tag{23}$$

and $\mathbf{u}$ is the incremental nodal displacement vector associated to the beam element defined as

$$\mathbf{u}^T = [u_1^1 \;\; u_2^1 \;\; u_3^1 \;\; v_1^1 \;\; v_2^1 \;\; v_3^1 \;\; u_1^2 \;\; u_2^2 \;\; u_3^2 \;\; v_1^2 \;\; v_2^2 \;\; v_3^2] \tag{24}$$

Using the interpolation matrix to evaluate Eq. (19), the global dynamic equilibrium equation in the matrix form is

$${}^{t+\Delta t}\ddot{} + {}^{t+\Delta t}\dot{} + ({}^{t}_{t} + {}^{t}_{t}) = {}^{t+\Delta t} - {}^{t}_{t} \tag{25}$$

where $\mathbf{M}$ is the global mass matrix, $\mathbf{D}$ is the global damping matrix, ${}^{t}_{t}$ L is the global linear incremental stiffness matrix, ${}^{t}_{t}$ L is the global nonlinear geometric stiffness matrix, ${}^{t+\Delta t}$ is the updated global vector of external nodal forces, ${}^{t}_{t}$ is the global vector of internal nodal forces, $\mathbf{U}$ is the global vector of incremental nodal displacements, and ${}^{t+\Delta t}\dot{\mathbf{U}}$ and ${}^{t+\Delta t}\ddot{}$ are the updated global nodal velocity and acceleration vectors, respectively. Table 1 summarizes these calculations.

Table 1
Integral form and corresponding matrix form of terms of Eq. (19).

Integral form	Matrix form
$\int_{0_V} {}^{0}\rho\, {}^{t+\Delta t}\ddot{u}_i \delta u_i d^0V$	${}^{t+\Delta t}\ddot{\mathbf{R}} = \sum_m [\int_{0_{V(m)}} {}^{0}\rho^{(m)} \mathbf{N}^{(m)T} \mathbf{N}^{(m)} d^0V^{(m)}]\, {}^{t+\Delta t}\ddot{\mathbf{U}}$
$\int_{0_V} k\, {}^{t+\Delta t}\dot{u}_i \delta u_i d^0V$	${}^{t+\Delta t}\dot{\mathbf{R}} = \sum_m [\int_{0_{V(m)}} {}^{0}k^{(m)} \mathbf{N}^{(m)T} \mathbf{N}^{(m)} d^0V^{(m)}]\, {}^{t+\Delta t}\dot{\mathbf{U}}$
$\int_{t_V} {}_t C_{ijrs}\, \Delta e_{rs}\, \delta \Delta e_{ij}\, d^tV$	${}_t^t\mathbf{K} = \sum_m [\int_{t_{V(m)}} {}_t^t\mathbf{B}^{(m)T}\, {}_t\mathbf{C}\, {}_t^t\mathbf{B}^{(m)} d^tV^{(m)}]$
$\int_{t_V} {}^t\tau_{ij}\, \delta \Delta \eta_{ij}\, d^tV$	${}_t^t\mathbf{K}_{\sigma} = \sum_m [\int_{t_{V(m)}} {}_t^t\mathbf{G}^{(m)T}\, {}_t\boldsymbol{\tau}\, {}_t^t\mathbf{G}^{(m)} d^tV^{(m)}]$
${}^{t+\Delta t}\mathbf{F} = \int_{0_S} {}_0^{t+\Delta t}f_i^S \delta u_i^S d^0S + \int_{0_V} {}_0^{t+\Delta t}f_i^B \delta u_i d^0V$	${}^{t+\Delta t}\mathbf{R} = \sum_m \int_{0_{S(m)}} \mathbf{N}^{S(m)T}\, {}_0^{t+\Delta t}\mathbf{f}^{S(m)} d^0S^{(m)} + \sum_m \int_{0_{V(m)}} \mathbf{N}^{(m)T}\, {}_0^{t+\Delta t}\mathbf{f}^{B(m)} d^0V^{(m)}$
$\int_{t_V} {}^t\tau_{ij}\, \delta \Delta e_{ij}\, d^tV$	${}_t^t\mathbf{F} = \sum_m \int_{t_{V(m)}} {}_t^t\mathbf{B}^{(m)T}\, {}_t\boldsymbol{\tau}^{(m)}\, d^tV^{(m)}$

A step-by-step time integration of the equilibrium equations was implemented with the HHT algorithm [7], and the numerical solution was obtained using the Newton-Raphson iterative technique [13].

3.3. Linear stiffness matrix

The linear strain components in Eq. (11) are defined at any point of the riser cross-section by

$$\begin{aligned} e_{11} &= u_{1,1} - x_2 v_{3,1} + x_3 v_{2,1} \\ 2e_{12} &= u_{2,1} - v_3 - x_3 v_{1,1} \\ 2e_{13} &= u_{3,1} - v_2 - x_2 v_{1,1} \end{aligned} \tag{26}$$

The first strain component e_{11} corresponds to the linear strain (extensional) in the direction ξ (Fig. 2), and components e_{12} and e_{13} refer to the shear strains (angular). The relation between the linear strains and the incremental nodal displacements is expressed in the matrix form using Eqs. (20) and (26) as

$$\mathbf{e} = [e_{11} \;\; 2e_{12} \;\; 2e_{13}]^T = \quad \mathbf{u} \tag{27}$$

where $_{\mathbf{L}}$ is the linear strain-displacement transformation matrix as defined in Appendix B.2.

The components of the Cauchy stress tensor ($\hat{}$) are related to the components of the linear strain tensor ($\mathbf{e}$) through the linear elastic constitutive matrix ($\mathbf{C}$) as

$$\hat{} = [\sigma_{11} \;\; \sigma_{12} \;\; \sigma_{13}]^T = \tag{28}$$

where

$$\mathbf{C} = \mathrm{diag}(E,\ G,\ G), \quad G = E/(2(1+\upsilon)) \tag{29}$$

In the constitutive matrix, E is the Young's modulus and υ is the Poisson's ratio.

Because we assume that the risers are made of a FGM, we use a non-homogeneous material model in which the elastic modulus, E, varies according to the following power law:

$$E = E_o (r/r_o)^{\beta}, \quad r_i \leqslant r \leqslant r_o \tag{30}$$

where β is a non-homogeneity parameter of the Young's modulus and $r = (x_2^2 + x_3^2)^{1/2}$ is used to refer to the radial coordinate through the pipe thickness.

The linear stiffness matrix $\mathbf{K_L}$ results from the discretization of the term $\int_V C_{ijrs} \Delta e_{rs} \delta \Delta e_{ij} dV$ in Eq. (19), as follows

$$\int_V C_{ijrs}\, \Delta e_{rs}\, \delta \Delta e_{ij}\, dV = \int_V (\delta \quad)^T \quad dV = (\delta \quad)^T \left(\int_V \quad^T \quad dV \right) \mathbf{u} \tag{31}$$

where $$= \int_V \quad^T \quad dV \tag{32}$$

After replacing Eq. (29) and $_{\mathbf{L}}$ in Eq. (32) and by integrating the volume of the riser element (Fig. 2), we obtain the final expression for the linear stiffness matrix. To calculate the volume integral of Eq. (32), it is convenient to convert the local co-rotated coordinate system of the riser element (ξ, x_2, x_3) to the cylindrical coordinate system (ξ, r, θ) by using the following transformations: $x_2 = r\cos\theta$, $x_3 = r\sin\theta$ and $r_i \leqslant r = (x_2^2 + x_3^2)^{1/2} \leqslant r_o$, which leads to

$$= \int_V \quad^T \quad dV = \int_0^{2\pi} \int_{r_i}^{r_o} \int_0^L \quad^T \quad r d\xi dr d\theta \tag{33}$$

where $\mathbf{K_L}$ is presented in Appendix B.3 in a closed form and is expressed as a function of the equivalent rigidity moduli (e.g., $\overline{EA}$, $\overline{EI}$, and $\overline{GJ}$).

3.4. Geometric stiffness matrix

The geometric stiffness matrix results from the discretization of the incremental (virtual) work done by the Cauchy stress tensor on the virtual strain increment (nonlinear part) in the incremental equilibrium equation (Eq. (19)),

$$\int_V \tau_{ij}\, \delta \Delta \eta_{ij}\, dV = \int_V \delta \quad^T \quad dV \tag{34}$$

where $\delta \quad^T = [\delta\eta_{11} \;\; \delta\eta_{12} \;\; \delta\eta_{13}]$ is the first variation of the nonlinear strain tensor and $\hat{}^T = [\sigma_{11} \;\; \sigma_{12} \;\; \sigma_{13}]$ is the vector of the updated Cauchy stress tensor components.

After some algebraic manipulations and making use of Eq. (20), we obtain the geometric stiffness matrix $\quad_{\mathbf{L}}$ as

$$\int_V \delta \quad^T \quad dV = (\delta \quad)^T \left(\int_V \quad^T \quad dV \right) \mathbf{u} \tag{35}$$

where $$= \int_0^{2\pi} \int_{r_i}^{r_o} \int_0^L \quad^T \quad r d\xi dr d\theta \tag{36}$$

and $\quad_{\mathbf{L}}$ is the nonlinear strain-displacement transformation matrix and $\boldsymbol{\tau}$ is the matrix of the updated Cauchy stress tensor components. Appendices B.4 and B.5 present $\quad_{\mathbf{L}}$ and $\boldsymbol{\tau}$ matrices explicitly.

3.5. Consistent mass matrix

The consistent mass matrix, $\mathbf{M}$, is obtained from the work done by the inertial forces in Eq. (19), as follows:

$$\int_V \rho\, {}^{t+\Delta t}\ddot{u}_i \delta u_i dV = (\delta \quad)^T \left(\int_V \rho \quad^T \quad dV \right) {}^{t+\Delta t}\ddot{\mathbf{u}} \tag{37}$$

$$= \int_0^{2\pi} \int_{r_i}^{r_o} \int_0^L \rho \quad^T \quad r d\xi dr d\theta \tag{38}$$

where $\quad$ is the element interpolation matrix (Eq. (23)) and ρ is the material density, which varies along the radial coordinate of the pipe cross-section according to the following power law

$$\rho = \rho_o (r/r_o)^{\alpha}, \quad r_i \leqslant r \leqslant r_o \tag{39}$$

where α is a non-homogeneity parameter of the material density. The consistent mass matrix $\mathbf{M}$ is shown in Appendix B.6 in a closed form.

3.6. Vector of external forces

The vector of external forces results from the discretization of the first and second terms on the right-hand side of Eq. (19) (virtual work done by loads acting on the riser). Thus

$$= \int_S \quad^{ST}\, {}_0^{t+\Delta t}\mathbf{f}^S dS + \int_V \quad^{T}\, {}_0^{t+\Delta t}\mathbf{f}^B dV \tag{40}$$

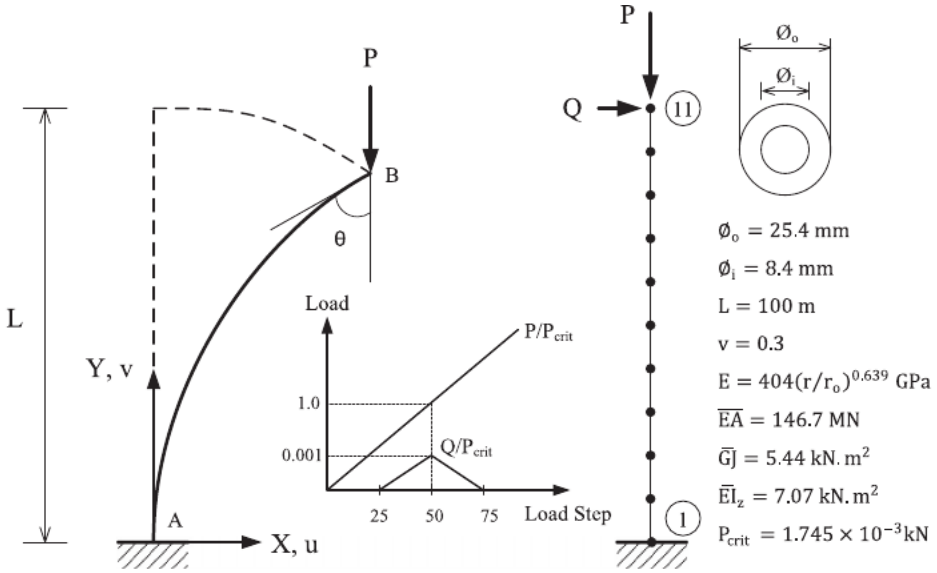

Fig. 4. Beam geometric, physical, and loading characteristics.

The external forces considered in this study were self-weight, buoyancy, hydrodynamic (owing to maritime waves, currents, and added mass inertia), prescribed displacements at the floating platform, action of floaters, and seabed-structure interactions (for further information about these external forces, see for example Ref. [7]).

4. Numerical results

The co-rotational approach for nonlinear analysis of FGM risers was implemented in a Fortran code and representative numerical (static and dynamics) examples were carried out to validate the element performance. The influence of material gradation on the numerical response in comparison with homogeneous material risers is discussed.

4.1. Static analyses

4.1.1. Cantilever beam under buckling

In this example, a cantilever FGM beam subject to a compressive centric force at the end of the tip is analyzed in a post-critical buckling condition. A small lateral force Q (0.1% of the compressive force P) is applied to move the column from its vertical position. The numerical input data used, including beam dimensions and material property parameters, are presented in Fig. 4. The Young's modulus varies along the radial direction of the pipe cross-section according to the power law $E(r) = 404(r/r_o)^{0.639}\ GPa$, having TiC and Ni$_3$Al at the external radius and inner radius, respectively.

The FGM column is modeled using 10 straight beam elements, the compression loading is applied in 400 equal increments, and the displacement tolerance is set to 0.001. The critical load for the first buckling mode is calculated by the Euler Formula [38] as $P_{crit} = \left(\frac{\pi^2}{4}\right)\left(\frac{EI_z}{L^2}\right) = 1.745$ N. Fig. 5 presents the deformed configurations of the column for different levels of compressive load ($P=\lambda P_{crit}$). The normalized tip displacements of the column for different values of P/P_{crit} ratio are shown in Fig. 6. The results are in good agreement with the solution presented by Timoshenko [38] for a homogeneous material.

Finally, Fig. 7 shows the results of the normal stress distributions at the clamped end of the beam for $\lambda = 2.19$. These longitudinal stresses are analytically evaluated using the expression

$$\sigma_{YY} = E(r)\varepsilon_{YY} = E(r)\left(-\frac{P}{A} + \frac{M_z x}{EI_z}\right) \tag{41}$$

where $P = 2.19P_{crit}$ and $M_z = -Pu_B$ (neglecting the contribution of the small force Q). Fig. 7a and b present normal stress distributions furnished by the numerical analysis for the FGM beam and by Eq. (41) along the beam for two different cross-section cuts: at a vertical cross-section and at 45° apart from this position, respectively. A very good agreement between these distributions is observed. Also, these results are compared to the stresses in a homogeneous beam cross-section having the same equivalent bending rigidity. For this particular loading, the plots show stress redistributions for the FGM material with 15% increase in the maximum longitudinal stress and a 43% decrease in its minimum value, as compared to the linear distributions shown in the homogeneous material beam.

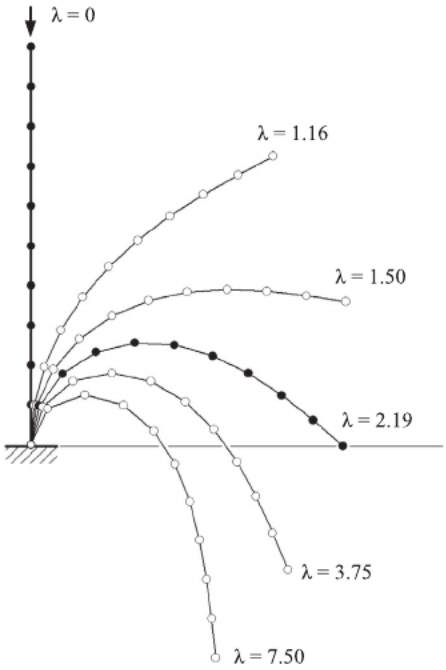

Fig. 5. Beam configurations for various tip loadings.

4.1.2. Cantilever arch beam under out-of-plane loading

This example proposed by Bathe and Bolourchi [13] aimed to evaluate the accuracy and robustness of the 3D beam element

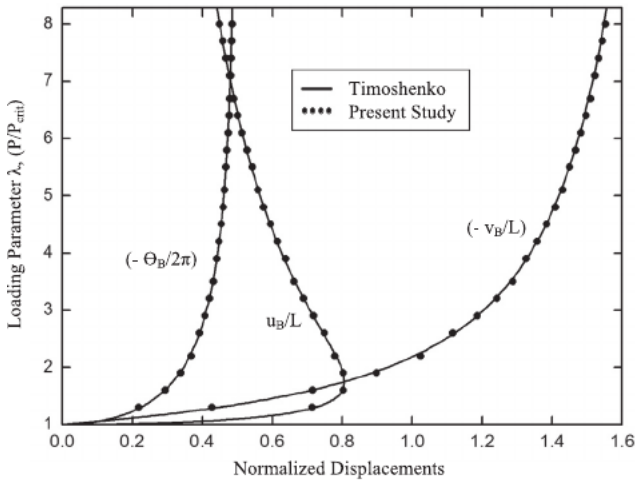

Fig. 6. Normalized numerical displacements as compared to Timoshenko's solution [38].

implemented with axial forces, bending, and torsion. The analysis considers a 45° cantilever arch beam with radius of 100 in measured from the centerline of the pipe subjected to a vertical end load, as shown in Fig. 8.

The model is idealized using eight equal straight-beam elements. The structure is subjected to a maximum load factor of $\lambda = 7.2$ which is applied in 60 equal increments. Fig. 9 shows the normalized tip displacements u_B, v_B, and w_B in the X, Y, and Z directions, respectively. A good agreement is observed between obtained numerical results and the solutions provided by Bathe and Bolourchi [13].

Fig. 10 shows the deformed configurations for three different loading levels and the tip displacements, which are compared to Bathe and Bolourchi [13].

4.1.3. Lee s frame

This well-known problem was proposed and solved analytically by Lee et al. [39] and has been studied elsewhere [14,40,41]. It is a benchmark problem to the validation of formulations for geometric nonlinear analysis and exhibits complex equilibrium paths featuring snap-through and snap-back phenomena. The FGM frame is composed

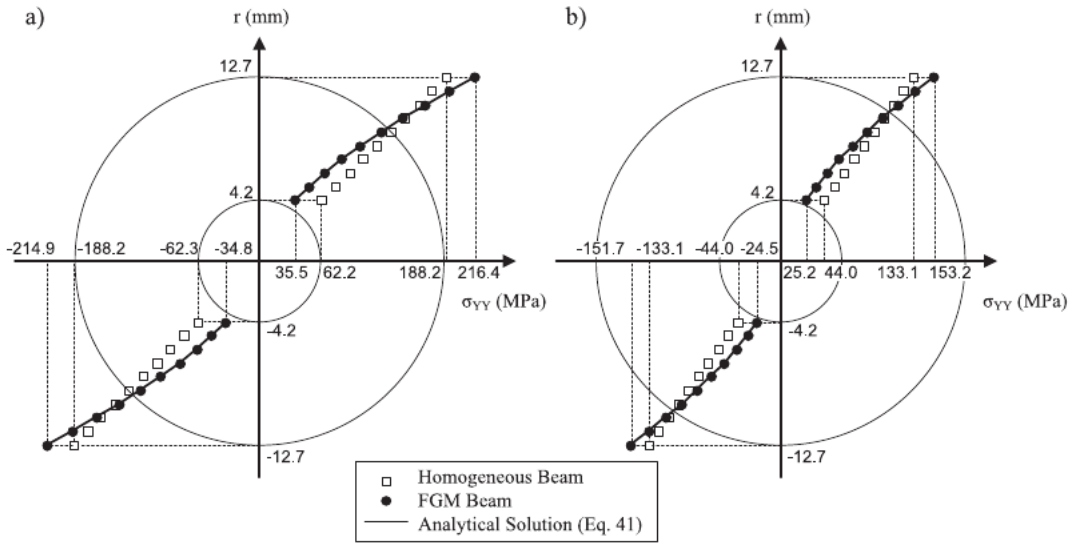

Fig. 7. Normal stresses at clamped end of beam ($\lambda = 2.19$, $E(r) = 404(r/r_0)^{0.639}$ GPa).

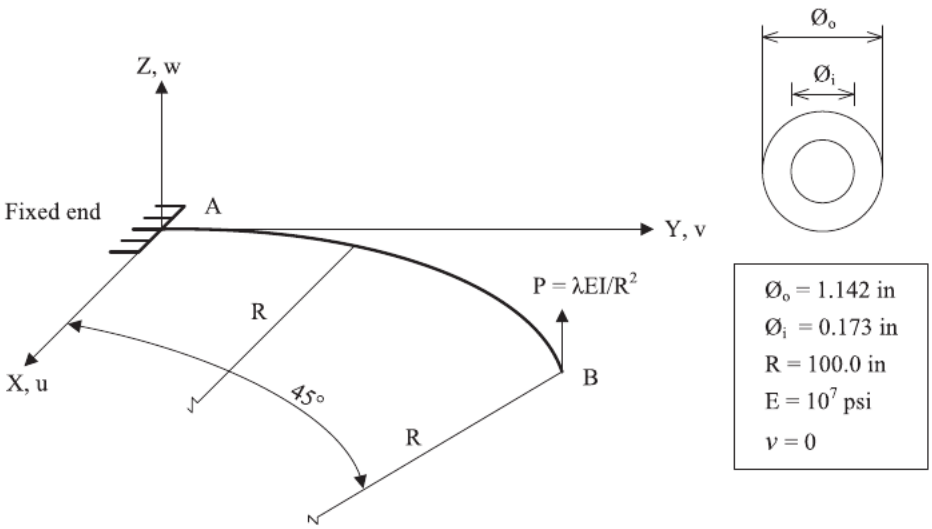

Fig. 8. Beam geometric, material (homogeneous), and loading characteristics.

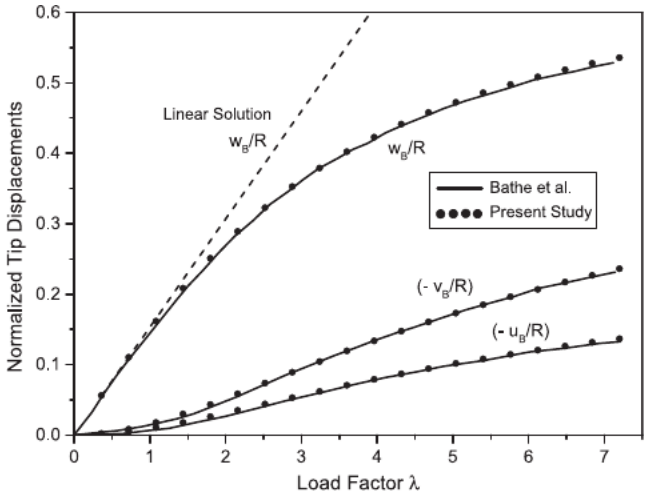

Fig. 9. Beam tip displacements for increasing transverse loading.

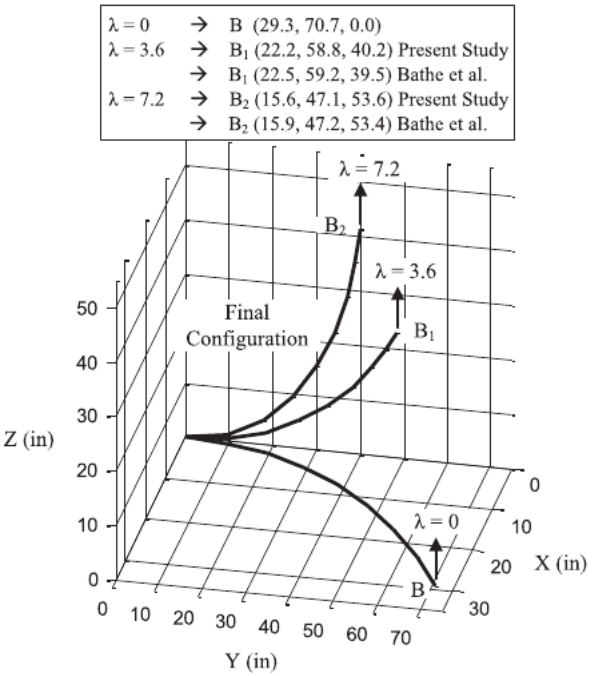

Fig. 10. Beam spatial configurations in large displacement analysis.

by the union of two beams under a vertical load P, with each structural member having a length of 1.2 m and pipe cross-section; the geometry and material parameters are shown in Fig. 11.

The frame is modeled using 20 equal-beam elements, and the numerical solution is obtained using the Generalized Displacement Control Method [40], which uses an incremental-iterative procedure with 590 steps, and the displacement tolerance is set to 0.001. The displacements u and v at the load application point are shown in Fig. 12.

Fig. 13 shows the deformed shape of the Lee frame for each of the uppercase letters A-E in Fig. 12. These results show the snap-back phenomena that occurs between the deformed configuration C and D. Figs. 14 and 15 show the deformed shapes B, C, D, and E.

Fig. 16 shows the normal Cauchy stress, σ_{xx}, at the deformed configuration A (cf. Fig. 13). As shown in the figure, the Cauchy stress is evaluated along two planes, 1–1′ and 2–2′, on the cross section. Similar to results shown in the previous example, the stress distribution obtained here varies smoothly along the radial direction of the pipe.

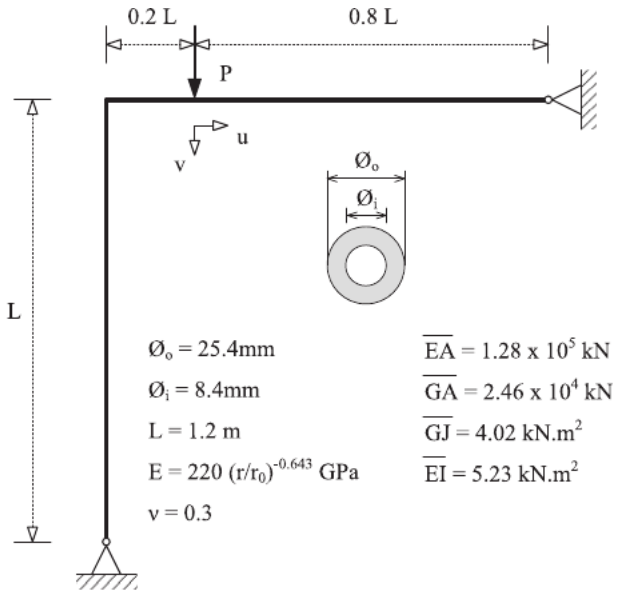

Fig. 11. Lee's frame input data.

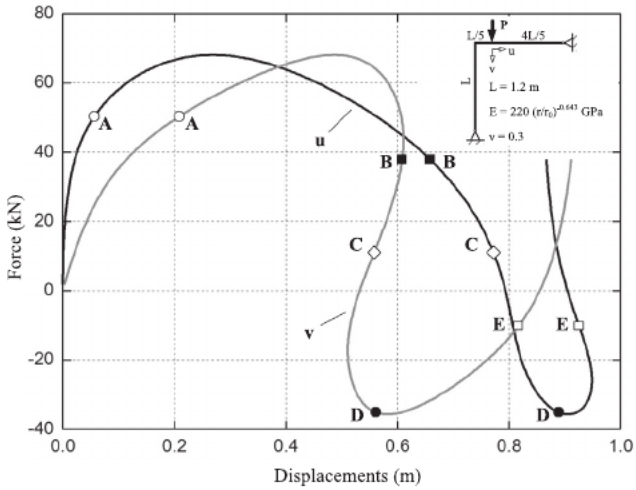

Fig. 12. Equilibrium paths for Lee's frame.

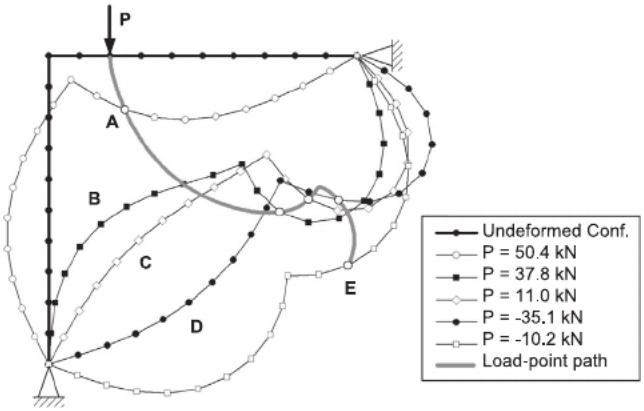

Fig. 13. Lee's frame deformed configurations.

4.1.4. Submerged cantilever riser under hydrostatic load

This example, proposed by Yazdchi and Crisfield [11], considers a flexible cantilever polyethylene riser of length 20 m under a vertical load at the tip. The riser is capped at the ends and submerged at a depth

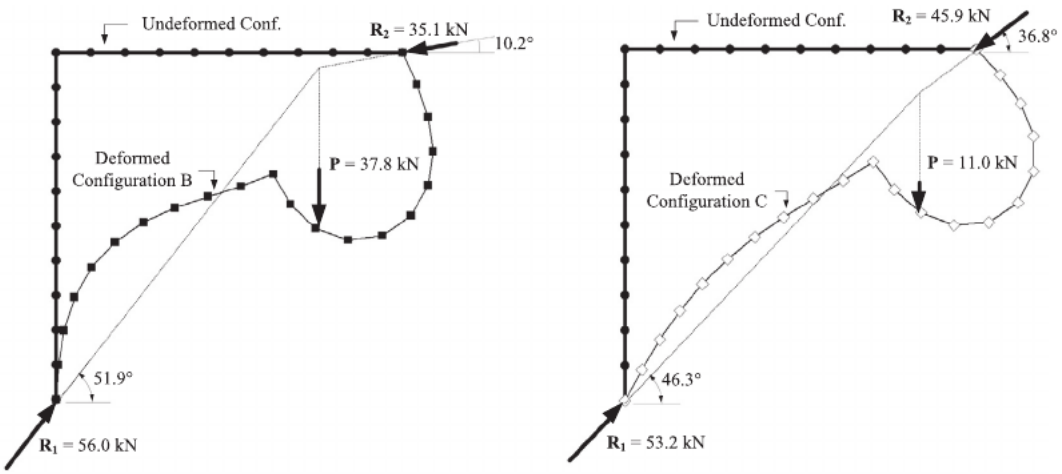

Fig. 14. Forces in equilibrium on deformed configurations B and C.

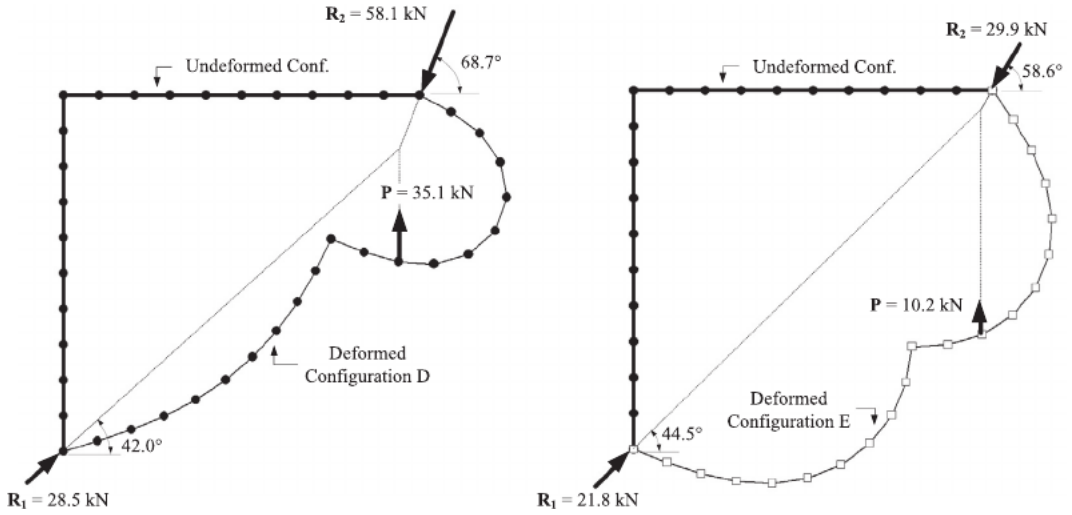

Fig. 15. Forces in equilibrium on deformed configurations D and E.

of 100 m. The mechanical and geometrical properties of the riser are shown in Fig. 17. The objective of this analysis is to verify the final equilibrium configuration of the riser subjected to the action of the self-weight, buoyancy, and a vertical tip load. The riser is modeled using 20 equally spaced elements, and the loading is applied in 50 equal increments. A displacement tolerance of 0.001 is used for the convergence in the Newton-Raphson iteration scheme. In every load step, the converged solution is obtained within four iterations.

Fig. 18 illustrates the deformed configurations for four loading conditions. In this figure, obtained numerical results show good agreement with [11].

4.1.5. Vertical riser under constant current and top tension force

The example proposed by Yazdchi and Crisfield [11] analyzed the behavior of a pre-tensioned riser under a 510 kN axial force caused by a floating system and a uniform current. The riser has a total length of 320 m but the water depth is 300 m. The material and geometrical parameters of the riser are shown in Fig. 19. This example considers a typical rigid riser system in the Top Tensioned Riser (TTR) configuration commonly used in both production and drilling on TLP and Spar platforms. The tension force at the top of the riser is necessary to avoid buckling due to self-weight.

The structure is modeled using 30 equally submerged elements and four equal elements above the water level. The loadings (self-weight, buoyancy, tension force, and current profile) are applied in 70 equal increments. Initially, the riser is in the vertical position with the bottom node being hinged and the top node allowed to move in the X-direction only. A displacement tolerance of 0.001 is used for the convergence in the Newton-Raphson iteration scheme. In every load step, the converged solution is obtained within three iterations. Fig. 20 shows two deformed riser configurations considering the magnitudes for the uniform current profile, specifically, 1.0 and 2.0 m/s. It is observed that the deformed configurations are not symmetrical because of the effect of current loading, and also because the tension force in the riser varies along the length, being smaller near the bottom because of its apparent weight. A good agreement is observed between the numerical solutions obtained in this study and those obtained by Yazdchi and Crisfield [11].

4.2. Dynamic analyses

4.2.1. Curved cantilever beam under a vertical load at tip

This example considers the dynamic analysis of the curved beam analyzed in Section 4.1.2. The finite element model uses 16 equally spaced straight elements, subjected to a sudden 300 lb vertical force for a total time of 0.3 s with a step time of 0.002 s. The physical, geometric, and loading parameters are shown in Fig. 21.

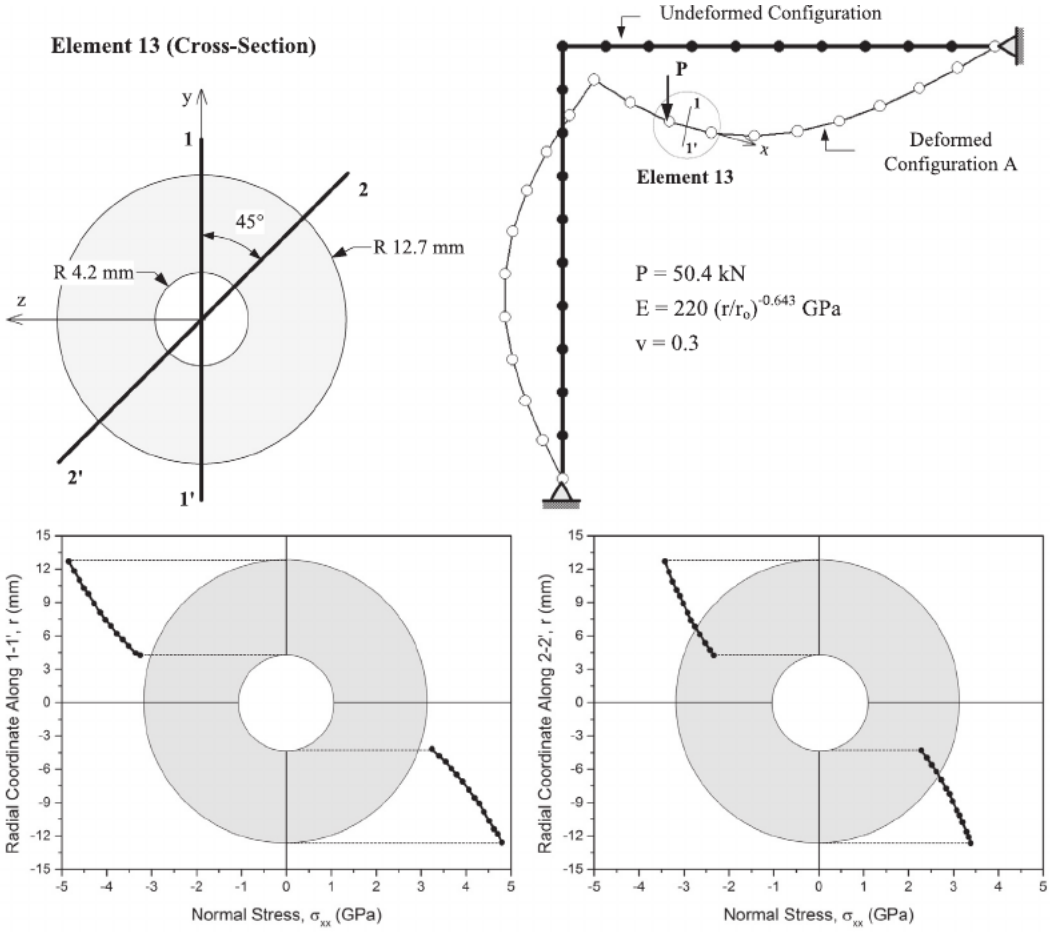

Fig. 16. Deformed configuration A and normal stresses on element 13 cross-section (along lines 1–1′ and 2–2′).

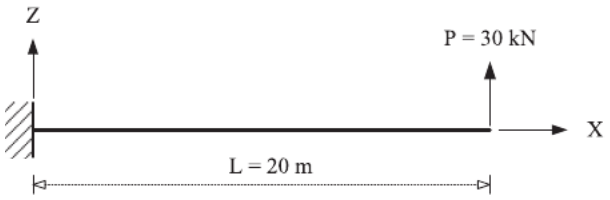

Young's Modulus, E	2 GPa
Poisson's Ratio, ν	0.25
Specific Weight (riser), γ_r	12.00 kN/m^3
Specific Weight (water), γ_w	10.25 kN/m^3
Inner Diam. (riser), $Ø_i$	0.80 m
Outer Diam. (riser), $Ø_0$	0.85 m

Fig. 17. Submerged cantilever riser.

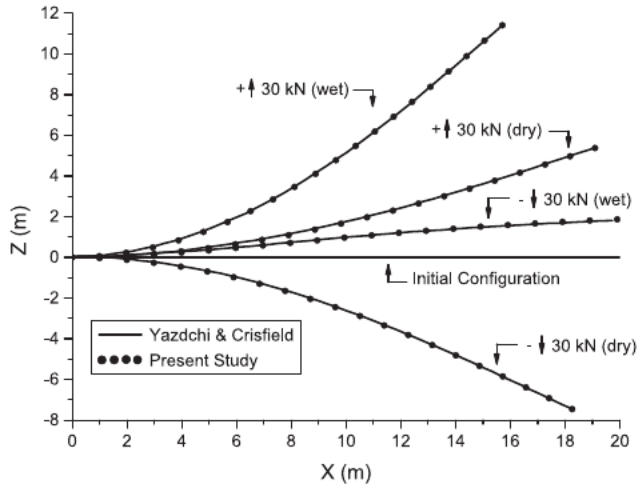

Fig. 18. Deformed configurations of cantilever riser.

The dynamic response of the tip displacements are plotted in Fig. 22. An excellent agreement is observed between the numerical results obtained with the proposed beam element and those obtained by Chan [42].

4.2.2. Large displacement static and dynamic analysis of a cantilever FGM beam subjected to distributed loading

In this example, originally proposed by Bathe et al. [43] for a homogeneous material beam, the objective is to test the FGM beam element undergoing large displacements under static and dynamic loadings. The current analysis assumes that the tube is made of a FGM with TiC at the inner surface of the pipe and Ni_3Al at its outer surface. Fig. 23 shows the physical and geometrical properties of the pipe, as well as the applied load intensities in the dynamic analysis (for a linear and non-linear behavior of the beam). In this analysis, the performance of the FGM beam is compared with TiC and Ni_3Al homogeneous beams. The beam is modeled using 10 equally spaced elements.

First, the static response of the beam is investigated. Then, a distributed load of maximum intensity equal to 30 kN/m is applied in time increments of the form q = 0.5t (kN/m, 0 t 60), where t is the time

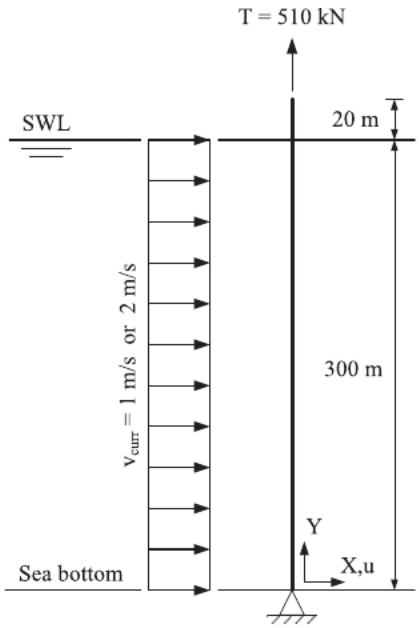

Young's Modulus, E	200 GPa
Poisson's Ratio	0.25
Specific weight (riser), γ_r	77 kN/m^3
Specific weight (water), γ_w	10.25 kN/m^3
Specific weight (int. fluid), γ_f	8 kN/m^3
Inner Diam. (riser), $\emptyset_i$	0.21 m
Outer Diam. (riser), $\emptyset_o$	0.25 m
Drag coef. (normal direction), C_{Dn}	1.00
Drag coef. (tangential direction), C_{Dt}	0.01

Fig. 19. Vertical riser input data.

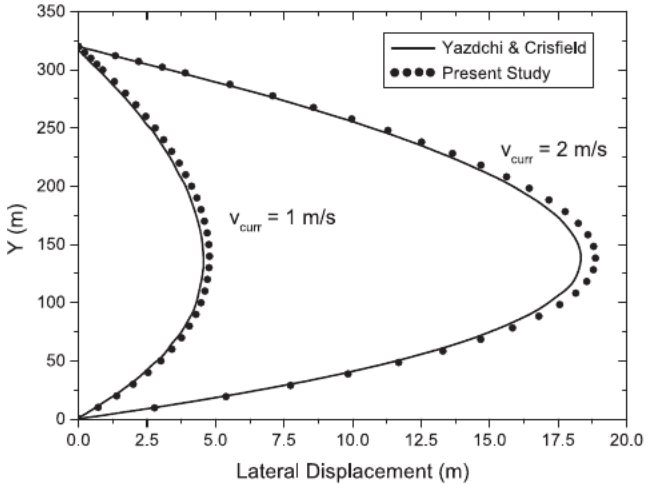

Fig. 20. Deformed configurations of vertical riser for two different current velocities.

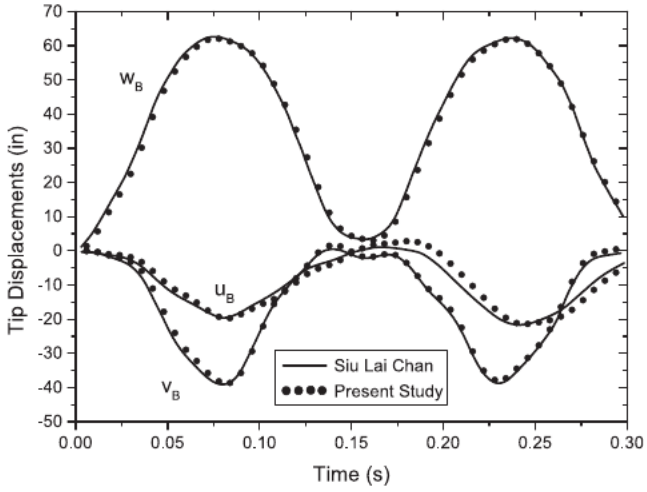

Fig. 22. Dynamic response of curved cantilever beam subjected to a tip load of 300 lb.

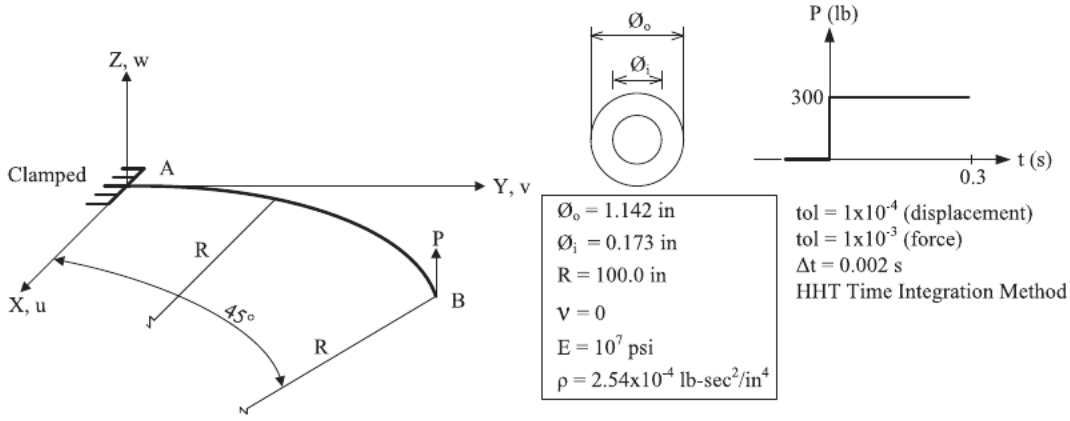

Fig. 21. Curved cantilever beam considered in analysis.

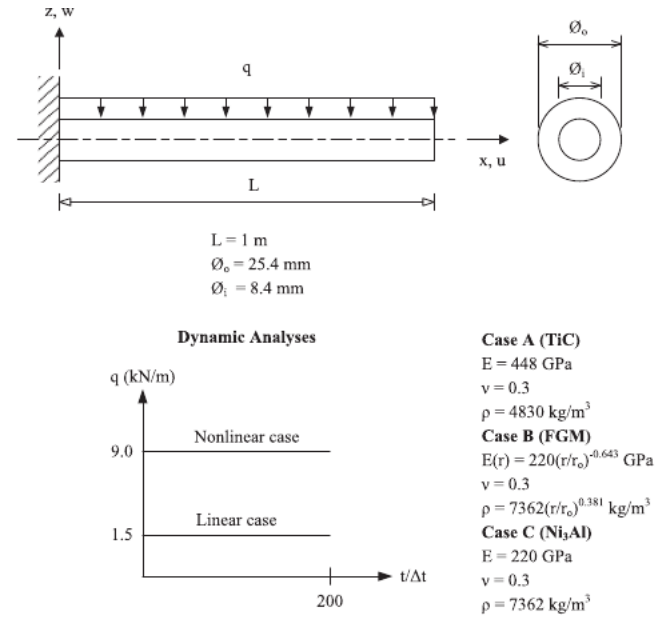

Fig. 23. Physical, geometric and load properties applied in analysis of cantilever beam.

step of the numerical analysis. The objective is to verify the correlation of the vertical displacement of the tip of the beam with respect to the distributed load applied during the entire loading interval for three types of material, including FGM. The numerical results obtained are shown in Fig. 24.

To consider the dynamic behavior of the beam in small displacements (linear analysis) and large displacements (non-linear analysis), the beam is loaded with distributed loads of magnitude 1.5 kN/m and 9 kN/m, respectively, which are applied using a Heaviside function, as shown in Fig. 23. Using the time increment of $\Delta t = 5E\ \ 4$ s, the solution of the problem is obtained until the instant 0.1 s. The convergence criterion is set to 1E 4 for displacements and 1E 3 for forces. The converged solution at each time step is obtained within three iterations. The linear and non-linear dynamic response for the tip vertical displacement for three types of materials: TiC, FGM, and Ni_3Al, are shown in Figs. 25 and 26, respectively. From the results, a delay is observed between the linear and non-linear dynamic responses due to the stiffening of the beam caused by the tension force in the beam with an increasing curvature. Consequently, the periods related to the first natural frequency in the non-linear analysis for the beam materials (i.e., TiC, FGM, and Ni_3Al) decreased with respect to the period obtained in the linear analysis. For the last two materials (FGM and Ni_3Al) this difference is more significant, corresponding to reductions in the order of 1.9% and 2.4%, respectively (see Table 2).

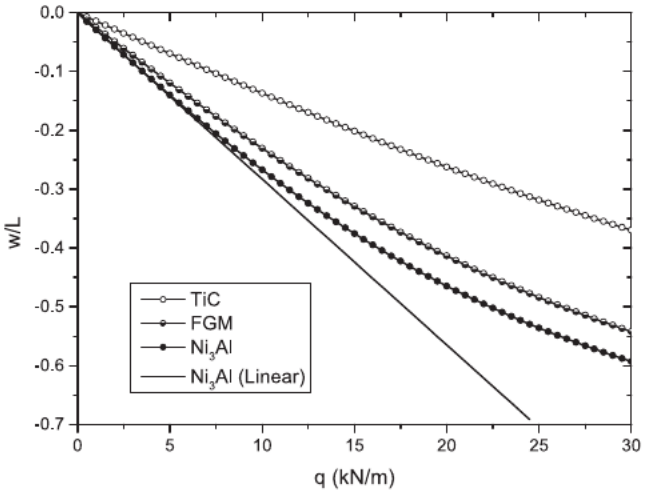

Fig. 24. Non-linear static analysis of cantilever beam.

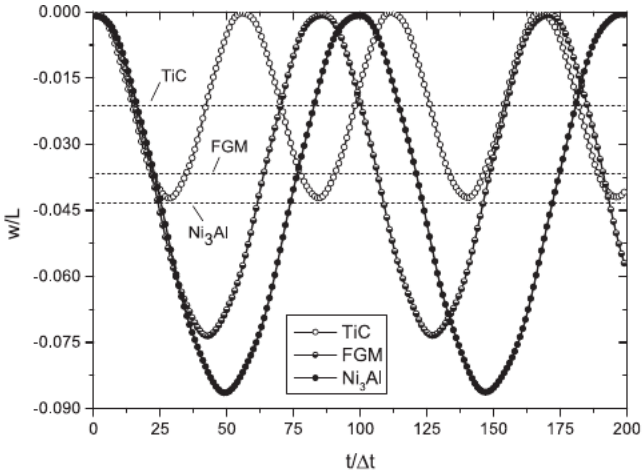

Fig. 25. Linear dynamic response of cantilever beam (dashed lines represent the static solutions).

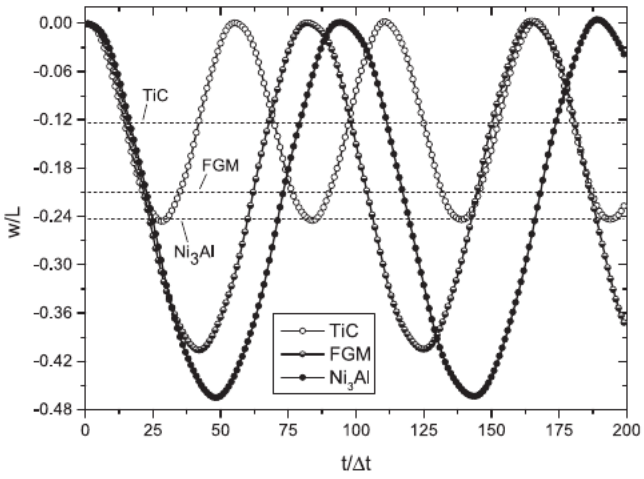

Fig. 26. Non-linear dynamic response of cantilever beam (dashed lines represent the static solutions).

4.2.3. Flexible riser in catenary configuration

This example studies the behavior of a flexible riser in a catenary configuration of length 350 m at a water depth of 150 m. One end of the riser is attached to a sub-sea tower at a depth of 150 m and the other end is connected to a ship horizontally displaced by 150 m. It is assumed that the riser is fully filled with seawater and hinged at both ends. The objective is to verify the accuracy of the beam element implemented in the riser analysis subjected to hydrodynamic loading and prescribed displacements of a ship's motion. The riser is modeled using 70 equally spaced elements, and the numerical results are compared with those obtained by Yadzdchi and Crisfield [12]. The geometry and

Table 2
Time period (in milliseconds) of dynamic responses.

Material	Linear analysis	Non-linear analysis
TiC	27.9	27.7
FGM	42.3	41.5
Ni_3Al	49.0	47.8

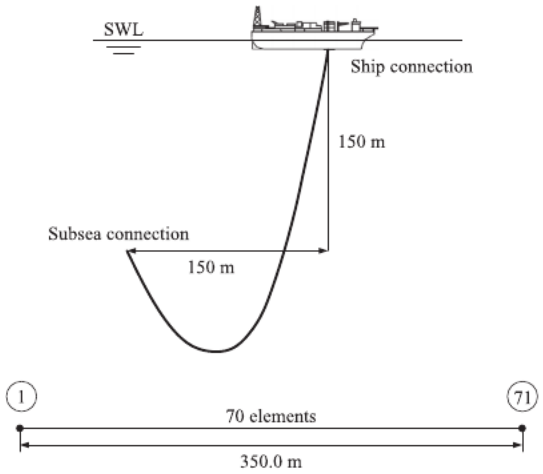

External diameter of the riser	0.26 m
Internal diameter of the riser	0.20 m
Bending stiffness of the riser, *EI*	20.96 x 10^3 N m^2
Axial stiffness of the riser, *EA*	15.38 x 10^8 N
Mass density of seawater, ρ_w	1025.0 kg/m^3
Mass per unit length of the riser	59.34 kg/m
Transverse drag coefficient, C_{DN}	1.0
Tangential drag coefficient, C_{DN}	0.0
Inertia coefficient, C_m	2.0
Time step, Δt	5 x 10^{-2} s
Wave heigth, *h*	20.0 m
Wave period, *T*	16.0 s
Surge motion of ship	
Amplitude	2.01 m
Period	14.0 s

Fig. 27. Flexible riser in catenary configuration.

physical properties of the riser, hydrodynamic coefficients, and other parameters used in the analysis are given in Fig. 27. It is assumed in this analysis that the riser material is linear elastic. From the data in Fig. 27, it can be seen that the magnitude of the axial stiffness is five orders of magnitude larger than the bending stiffness. Hence, the flexible riser presented a structural behavior equivalent to a cable.

The analysis is divided in two parts: a static analysis, in which the riser deforms from an initially horizontal position until it connects to the ship on the surface, and a dynamic analysis, in which the tip of the riser moves due to the ship motion caused by waves. In the static analysis, the riser, initially in a horizontal position and located 150 m below sea level, is subjected to loads due to self-weight and buoyancy. The dashed line in Fig. 28 illustrates this configuration. Next, the right endpoint of the riser is connected to a ship located 150 m to the right of the sub-sea tower. This motion is applied incrementally, and the deformed configurations for intermediate installations are shown in Fig. 28. The horizontal and vertical reactions obtained at the support points are listed in Fig. 28. The reactions are compared with the values obtained by Yazdchi and Crisfield [12] that used a beam model and those obtained by McNamara et al. [44] with cable theory, and a good agreement is observed between the results.

The bending moment diagram along the riser in the final configuration (solid bold line in Fig. 28) is shown in Fig. 29; the results obtained agree with results reported in the literature [12,44].

The dynamic analysis under the action of forces owing to a ship's motion and waves is developed for two different cases:

(a) In the first case, only the surge movement of the ship is considered to investigate the nonlinear effects of the riser response compared to those obtained by Yazdchi and Crisfield [12]. The top of the riser is excited with a surge amplitude of 2.01 m and period of 14.0 s. The results of this analysis are represented in Figs. 30 and 31 for the vertical reactions at nodes 1 and 71, respectively. The vertical reaction obtained for node 1 occurs between 35.73 and 35.94 kN; however, in the results obtained in [12], this reaction are in 35.64–36.07 kN range. A very good agreement in the period and in the average value of the harmonic function is observed. However, the obtained amplitudes are 51% of those obtained in [12]. High-order harmonics are also observed at this node. In the case of the vertical reaction at node 71, an excellent agreement is observed between the numerical results (amplitude and period) obtained in the study and those obtained in [12].
(b) In the second case, in addition to the surge movement of the ship, a harmonic wave with period of 16 s and amplitude of 20.0 m is applied. The results for this case are shown in Figs. 30 and 31. A good agreement is observed with the results obtained in [12].

Support Reactions	V_1 (kN)	V_{71} (kN)	H_1 (kN)	H_{71} (kN)
Yazdchi & Crisfield	35.86	91.61	12.04	12.04
McNamara et al.	35.77	91.51	12.02	12.02
Present Study	35.83	91.64	12.03	12.03

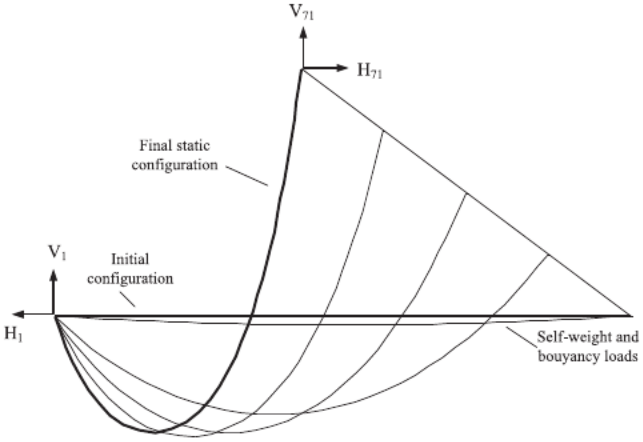

Fig. 28. Installation process of riser and support reactions.

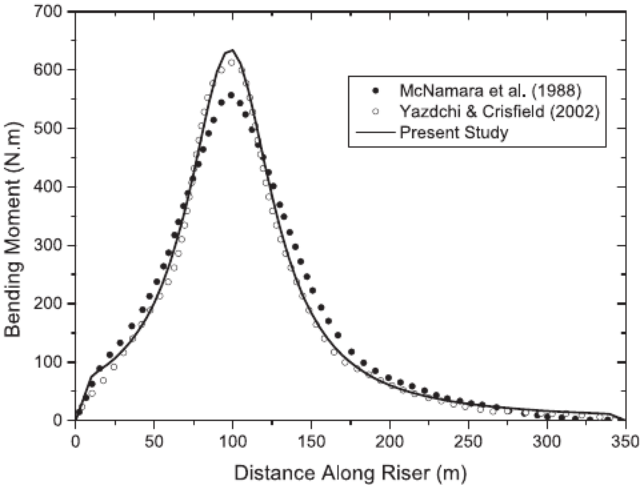

Fig. 29. Static bending moment distribution along riser.

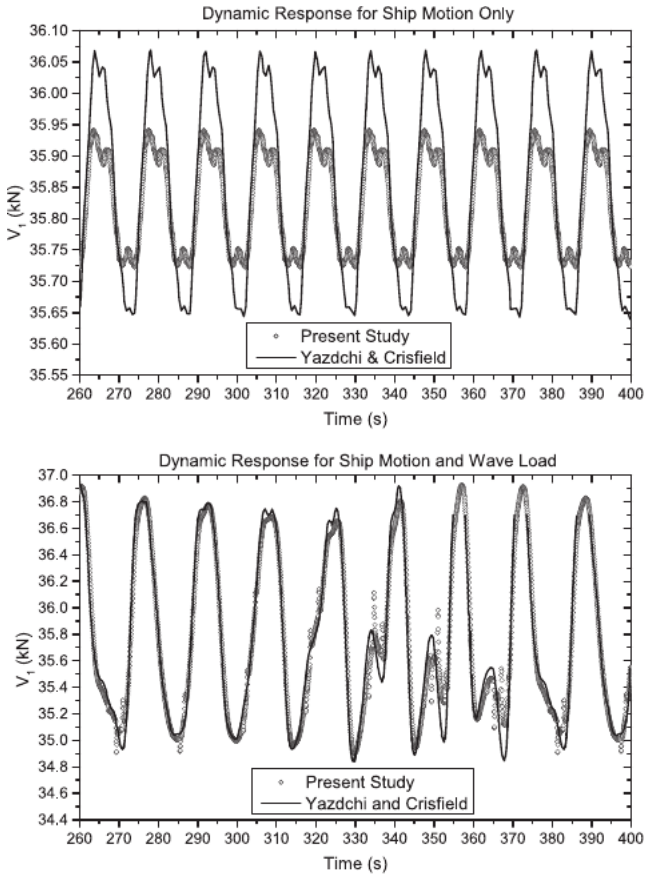

Fig. 30. Vertical reaction at subsea connection.

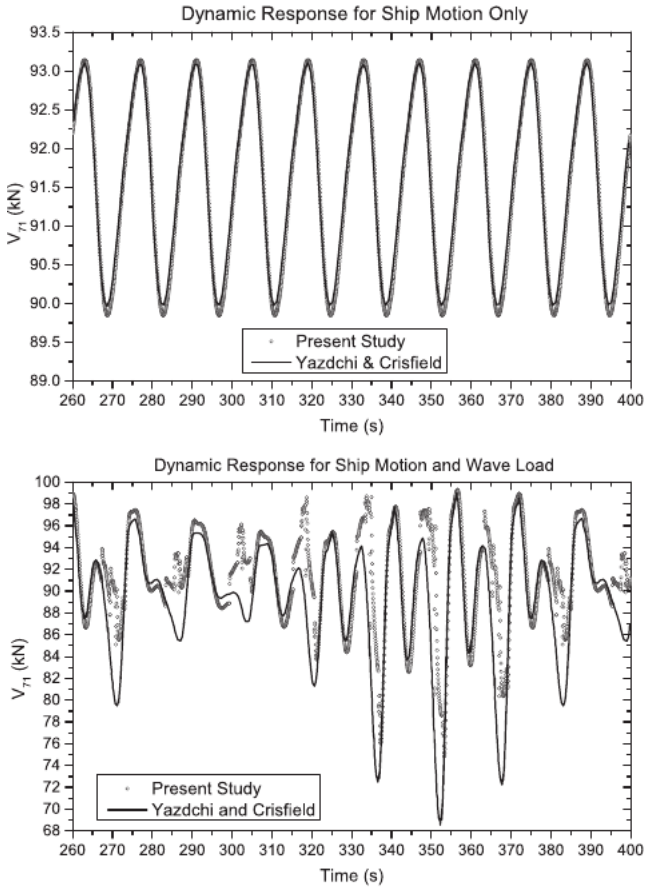

Fig. 31. Vertical reaction at ship connection.

In the dynamic analysis, the equations of motion are integrated in the interval of 400 s using a time increment of $\Delta t = 0.05$ s. The convergence criterion is set to 1E 3 for displacements and 1E 2 for forces. An average of three and four iterations per time step are necessary to reach the convergence for the analyzes considering the ship motion only and considering the effect of the ship and waves, respectively.

5. Concluding remarks

In this study, we present a co-rotational formulation for a general two-node beam element in 3D, which we use for the non-linear dynamic analysis of flexible marine risers made of functionally-graded materials. The material properties are assumed to vary in the radial direction according to a power law, and the effect of material gradation on the stiffness and mass matrices, as well as on the internal force vector, are all evaluated in closed form.

Several verification examples are presented, showing that both static and dynamic solutions are in good agreement with solutions available in the literature. The numerical examples reveal significant differences in stress distributions, as compared to those obtained for risers made of homogeneous materials, which suggests that FGMs can be used for the efficient design of flexible marine risers.

Acknowledgments

JCRA is thankful for the financial support provided by CNPq and the Pontifical Catholic University of Rio de Janeiro. GHP acknowledges support from the Raymond Allen Jones Chair at the Georgia Institute of Technology. The authors are grateful to useful and detailed comments provided by Mr. Oliver Giraldo-Londoño, which contributed to substantially improve the manuscript.

Appendix A. Nomenclature

t	time;
X_C, Y_C, Z_C	co-rotated coordinate system;
x_1, y_1, z_1	nodal reference system; local coordinates on element cross section;
$\boldsymbol{\Psi}$	pseudo vector of rotation;
v_1, v_2, v_3	components of rotations about X_C, Y_C and Z_C axis;
$\mathbf{u}$	displacement increment vector;
u_1, u_2, u_3	components of displacements in the X_C, Y_C and Z_C directions, respectively;
ξ	element coordinate in the longitudinal (X_C) direction;
ϕ_i	finite element shape functions for beams;
L	element length;
	interpolation matrix;
$\mathbf{M}$	mass matrix;
$\mathbf{D}$	damping matrix;
$\mathbf{U}$	global displacement vector;
$\dot{\mathbf{U}}$	global velocity vector;
$\ddot{\mathbf{U}}$	global acceleration vector;
e_{11}, e_{12}, e_{13}	linear strain components;
η_{11}, η_{12}, η_{13}	nonlinear strain components;
$_{\mathbf{L}}$	linear strain–displacement transformation matrix;
$_{\mathbf{L}}$	nonlinear strain–displacement transformation matrix;
$\mathbf{K}_{\mathbf{L}}$	linear stiffness matrix;
$_{\mathbf{L}}$	nonlinear stiffness matrix;
E	Young's modulus;
υ	Poisson's ratio;
ρ	material density;
α	non-homogeneity parameter of the material density;
β	non-homogeneity parameter of the Young's modulus;
$\overline{EA}$	equivalent axial rigidity;
$\overline{EI}$	equivalent flexural rigidity;
$\overline{GJ}$	equivalent torsional rigidity

Appendix B. Shape functions and element matrices

B.1. Finite element shape functions for beams

$$\phi_1(\xi) = 1-\frac{\xi}{L}, \quad \phi_2(\xi) = \frac{\xi}{L}, \quad \phi_3(\xi) = 1-3\left(\frac{\xi}{L}\right)^2 + 2\left(\frac{\xi}{L}\right)^3,$$
$$\phi_4(\xi) = 3\left(\frac{\xi}{L}\right)^2-2\left(\frac{\xi}{L}\right)^3, \quad \phi_5(\xi) = \left[\frac{\xi}{L}-2\left(\frac{\xi}{L}\right)^2 + \left(\frac{\xi}{L}\right)^3\right]L,$$
$$\phi_6(\xi) = \left[\left(\frac{\xi}{L}\right)^2-\left(\frac{\xi}{L}\right)^3\right]L, \quad \phi_7(\xi) = \frac{6}{L}\left[-\frac{\xi}{L} + \left(\frac{\xi}{L}\right)^2\right]$$
$$\phi_8(\xi) = 1-4\frac{\xi}{L} + 3\left(\frac{\xi}{L}\right)^2, \quad \phi_9(\xi) = 2\frac{\xi}{L}-3\left(\frac{\xi}{L}\right)^2 \tag{B.1}$$

B.2. Linear strain-displacement transformation matrix

$$= \begin{bmatrix} \frac{d\phi_1}{d\xi} & -x_2\frac{d\phi_7}{d\xi} & -x_3\frac{d\phi_7}{d\xi} & 0 & x_3\frac{d\phi_8}{d\xi} & -x_2\frac{d\phi_8}{d\xi} & \frac{d\phi_2}{d\xi} & x_2\frac{d\phi_7}{d\xi} & x_3\frac{d\phi_7}{d\xi} & 0 & -x_3\frac{d\phi_9}{d\xi} & x_2\frac{d\phi_9}{d\xi} \\ 0 & 0 & 0 & -x_3\frac{d\phi_1}{d\xi} & 0 & 0 & 0 & 0 & 0 & -x_3\frac{d\phi_2}{d\xi} & 0 & 0 \\ 0 & 0 & 0 & x_2\frac{d\phi_1}{d\xi} & 0 & 0 & 0 & 0 & 0 & x_2\frac{d\phi_2}{d\xi} & 0 & 0 \end{bmatrix}_{3\times 12} \tag{B.2}$$

B.3. Linear stiffness matrix

$$\mathbf{K_L} = \begin{bmatrix} \frac{\overline{EA}}{L} & 0 & 0 & 0 & 0 & 0 & -\frac{\overline{EA}}{L} & 0 & 0 & 0 & 0 & 0 \\ & \frac{12\overline{EI}}{L^3} & 0 & 0 & 0 & \frac{6\overline{EI}}{L^3} & 0 & -\frac{12\overline{EI}}{L^2} & 0 & 0 & 0 & \frac{6\overline{EI}}{L^2} \\ & & \frac{12\overline{EI}}{L^3} & 0 & -\frac{6\overline{EI}}{L^2} & 0 & 0 & 0 & -\frac{12\overline{EI}}{L^3} & 0 & -\frac{6\overline{EI}}{L^2} & 0 \\ & & & \frac{\overline{GJ}}{L} & 0 & 0 & 0 & 0 & 0 & -\frac{\overline{GJ}}{L} & 0 & 0 \\ & & & & \frac{4\overline{EI}}{L} & 0 & 0 & 0 & \frac{6\overline{EI}}{L^2} & 0 & \frac{2\overline{EI}}{L} & 0 \\ & & & & & \frac{4\overline{EI}}{L} & 0 & -\frac{6\overline{EI}}{L^2} & 0 & 0 & 0 & \frac{2\overline{EI}}{L} \\ & & & & & & \frac{\overline{EA}}{L} & 0 & 0 & 0 & 0 & 0 \\ & & & & & & & \frac{12\overline{EI}}{L^3} & 0 & 0 & 0 & -\frac{6\overline{EI}}{L^2} \\ & & & & & & & & \frac{12\overline{EI}}{L^3} & 0 & \frac{6\overline{EI}}{L^2} & 0 \\ & & & & & & & & & \frac{\overline{GJ}}{L} & 0 & 0 \\ & & & & & & & & & & \frac{4\overline{EI}}{L} & 0 \\ & & & & & & & & & & & \frac{4\overline{EI}}{L} \end{bmatrix}_{12\times 12} \tag{B.3}$$

with:

$$\overline{EA} = \int_A E_o r^\beta dA = \left(\frac{2\pi E_o r_o^2}{\beta + 2}\right)\left[1-\left(\frac{r_i}{r_o}\right)^{\beta+2}\right]$$

$$\overline{EI} = \int_A E_o x_2^2 r^\beta dA = \left(\frac{\pi E_o r_o^4}{\beta + 4}\right)\left[1-\left(\frac{r_i}{r_o}\right)^{\beta+4}\right]$$

$$\overline{GJ} = \int_A \frac{E_o r^\beta}{2(1+\nu)} r^2 dA = \frac{\pi E_o r_o^4}{(1+\nu)(\beta+4)}\left[1-\left(\frac{r_i}{r_o}\right)^{\beta+4}\right]$$

B.4. Nonlinear strain-displacement transformation matrix

$$= \begin{bmatrix} 0 & 0 & 0 & \phi_1 & 0 & 0 & 0 & 0 & 0 & \phi_2 & 0 & 0 \\ 0 & 0 & -\phi_7 & 0 & \phi_8 & 0 & 0 & 0 & \phi_7 & 0 & -\phi_9 & 0 \\ 0 & \phi_7 & 0 & 0 & 0 & \phi_8 & 0 & -\phi_7 & 0 & 0 & 0 & -\phi_9 \\ 0 & \frac{d\phi_3}{d\xi} & 0 & 0 & 0 & \frac{d\phi_5}{d\xi} & 0 & \frac{d\phi_4}{d\xi} & 0 & 0 & 0 & -\frac{d\phi_6}{d\xi} \\ 0 & 0 & \frac{d\phi_3}{d\xi} & 0 & -\frac{d\phi_5}{d\xi} & 0 & 0 & 0 & \frac{d\phi_4}{d\xi} & 0 & \frac{d\phi_6}{d\xi} & 0 \\ 0 & 0 & 0 & \frac{d\phi_1}{d\xi} & 0 & 0 & 0 & 0 & 0 & \frac{d\phi_2}{d\xi} & 0 & 0 \\ 0 & 0 & -\frac{d\phi_7}{d\xi} & 0 & \frac{d\phi_8}{d\xi} & 0 & 0 & 0 & \frac{d\phi_7}{d\xi} & 0 & -\frac{d\phi_9}{d\xi} & 0 \\ 0 & \frac{d\phi_7}{d\xi} & 0 & 0 & 0 & \frac{d\phi_8}{d\xi} & 0 & -\frac{d\phi_7}{d\xi} & 0 & 0 & 0 & -\frac{d\phi_9}{d\xi} \end{bmatrix}_{8\times 12} \tag{B.4}$$

B.5. Matrix of the updated Cauchy stress-tensor components

$$\tau = \begin{bmatrix} 0 & \frac{\sigma_{12}}{2} & \frac{\sigma_{13}}{2} & -\sigma_{13} & \sigma_{12} & 0 & \frac{\sigma_{11}x_2}{2} & \frac{\sigma_{11}x_3}{2} \\ & 0 & 0 & 0 & 0 & \frac{\sigma_{11}x_2}{2} & 0 & \frac{\sigma_{12}x_3-\sigma_{13}x_2}{2} \\ & & 0 & 0 & 0 & \frac{\sigma_{11}x_3}{2} & \frac{-\sigma_{12}x_3+\sigma_{13}x_2}{2} & 0 \\ & & & \sigma_{11} & 0 & -\sigma_{11}x_3 & 0 & 0 \\ & & & & \sigma_{11} & \sigma_{11}x_2 & 0 & 0 \\ & & & & & \sigma_{11}\left(x_2^2+x_3^2\right) & 0 & 0 \\ & & \text{symmetric} & & & & \sigma_{11}x_3^2 & -\sigma_{11}x_2x_3 \\ & & & & & & & \sigma_{11}x_2^2 \end{bmatrix}_{8\times 8} \tag{B.5}$$

B.6. Consistent mass matrix

$$\mathbf{M} = \begin{bmatrix} M_{1,1} & 0 & 0 & 0 & 0 & 0 & M_{1,7} & 0 & 0 & 0 & 0 & 0 \\ & M_{2,2} & 0 & 0 & 0 & M_{2,6} & 0 & M_{2,8} & 0 & 0 & 0 & M_{2,12} \\ & & M_{3,3} & 0 & M_{3,5} & 0 & 0 & 0 & M_{3,9} & 0 & M_{3,11} & 0 \\ & & & M_{4,4} & 0 & 0 & 0 & 0 & 0 & M_{4,10} & 0 & 0 \\ & & & & M_{5,5} & 0 & 0 & 0 & M_{5,9} & 0 & M_{5,11} & 0 \\ & & & & & M_{6,6} & 0 & M_{6,8} & 0 & 0 & 0 & M_{6,12} \\ & & & & & & M_{7,7} & 0 & 0 & 0 & 0 & 0 \\ & & & & & & & M_{8,8} & 0 & 0 & 0 & M_{8,12} \\ & & & & & & & & M_{9,9} & 0 & M_{9,11} & 0 \\ & & & & \text{symmetric} & & & & & M_{10,10} & 0 & 0 \\ & & & & & & & & & & M_{11,11} & 0 \\ & & & & & & & & & & & M_{12,12} \end{bmatrix}_{12\times 12} \tag{B.6}$$

with:

$$M_{1,1} = \frac{\overline{m}}{3}, \quad M_{1,7} = \frac{\overline{m}}{6}, \quad M_{2,2} = \left(\frac{13}{35} + \frac{6k^2}{5L^2}\right)\overline{m}, \quad M_{2,6} = \left(\frac{11L}{210} + \frac{k^2}{10L}\right)\overline{m}, \quad M_{2,8} = \left(\frac{9}{70} - \frac{6k^2}{5L^2}\right)\overline{m},$$

$$M_{2,12} = \left(-\frac{13L}{420} + \frac{k^2}{10L}\right)\overline{m}, \quad M_{3,3} = M_{2,2}, \quad M_{3,5} = -M_{2,6}, \quad M_{3,9} = M_{2,8}, \quad M_{3,11} = -M_{2,12},$$

$$M_{4,4} = \frac{\overline{m}}{3}k_r^2, \quad M_{4,10} = \frac{\overline{m}}{6}k_r^2, \quad M_{5,5} = \left(\frac{L^2}{105} + \frac{2k^2}{15}\right)\overline{m}, \quad M_{5,9} = M_{2,12}, \quad M_{5,11} = \left(-\frac{L^2}{140} - \frac{k^2}{30}\right)\overline{m},$$

$$M_{6,6} = M_{5,5}, \quad M_{6,8} = -M_{2,12}, \quad M_{6,12} = M_{5,11}, \quad M_{7,7} = M_{1,1}, \quad M_{8,8} = M_{2,2}, \quad M_{8,12} = -M_{2,6},$$

$$M_{9,9} = M_{2,2}, \quad M_{9,11} = M_{2,6}, \quad M_{10,10} = M_{4,4}, \quad M_{11,11} = M_{5,5}, \quad M_{12,12} = M_{5,5},$$

$$\overline{m} = \frac{2\pi\rho_o r_o^2}{\alpha+2}\left[1-\left(\frac{r_i}{r_o}\right)^{\alpha+2}\right], \quad k^2 = \frac{1}{2}\left(\frac{\alpha+2}{\alpha+4}\right)\left(\frac{r_o^{\alpha+4}-r_i^{\alpha+4}}{r_o^{\alpha+2}-r_i^{\alpha+2}}\right), \quad k_r^2 = 2k^2$$

Appendix C. Supplementary material

Supplementary data associated with this article can be found, in the online version, at http://dx.doi.org/10.1016/j.engstruct.2018.05.092.

References

[1] Howell CT. Numerical analysis of 2-d nonlinear cable equations with applications to low-tension problems. Int Soc Offsh Polar Engin 1992;2:110–3.
[2] Ohtsubo H, Watanabe O. Stress analysis of pipe bends by ring elements. J Press Vess Technol 1978;100(1):112–22. http://dx.doi.org/10.1115/1.3454422.
[3] Bathe K-J, Almeida CA, Ho LW. A simple and effective pipe elbow element some nonlinear capabilities. Comp Struct 1983;17(5):659–67. http://dx.doi.org/10.1016/0045-7949(83)90079-2.
[4] Fan H, Li C, Wang Z, Xu L, Wang Y, Feng X. Dynamic analysis of a hang-off drilling riser considering internal solitary wave and vessel motion. J Nat Gas Sci Eng 2017;37:512–22. http://dx.doi.org/10.1016/j.jngse.2016.12.003.
[5] Adamiec-Wjcik I, Brzozowska L, Drg ukasz. An analysis of dynamics of risers during vessel motion by means of the rigid finite element method. Ocean Eng 2015;106:102–14. http://dx.doi.org/10.1016/j.oceaneng.2015.06.053.
[6] Neto AG, Malta ER, de Mattos Pimenta P. Catenary riser sliding and rolling on seabed during induced lateral movement. Marine Struct 2015;41:223–43. http://dx.doi.org/10.1016/j.marstruc.2015.02.001.
[7] Aguiar L, Almeida C, Paulino G. Dynamic analysis of risers using a novel multi-layered pipe beam element model. Mar Struct 2015;44:211–31. http://dx.doi.org/10.1016/j.marstruc.2015.08.004.
[8] Aguiar L, Almeida C, Paulino G. A three-dimensional multilayered pipe beam element: nonlinear analysis. Comp Struct 2014;138:142–61. http://dx.doi.org/10.1016/j.compstruc.2013.09.005.
[9] Kordkheili SH, Bahai H, Mirtaheri M. An updated lagrangian finite element formulation for large displacement dynamic analysis of three-dimensional flexible riser structures. Ocean Eng 2011;38(5):793–803. http://dx.doi.org/10.1016/j.oceaneng.2011.02.001.
[10] Athisakul C, Monprapussorn T, Chucheepsakul S. A variational formulation for three-dimensional analysis of extensible marine riser transporting fluid. Ocean Eng 2011;38(4):609–20. http://dx.doi.org/10.1016/j.oceaneng.2010.12.012.
[11] Yazdchi M, Crisfield MA. Buoyancy forces and the 2d finite element analysis of flexible offshore pipes and risers. Int J Numer Meth Eng 2002;54(1):61–88. http://dx.doi.org/10.1002/nme.415.
[12] Yazdchi M, Crisfield MA. Nonlinear dynamic behaviour of flexible marine pipes and risers. Int J Numer Meth Eng 2002;54(9):1265–308. http://dx.doi.org/10.1002/nme.566.
[13] Bathe K, Bolourchi S. Large displacement analysis of three-dimensional beam structures. Int J Numer Meth Eng 1979;14(7):961–86. http://dx.doi.org/10.1002/nme.1620140703.
[14] Pacoste C, Eriksson A. Beam elements in instability problems. Comp Meth Appl Mech Eng 1997;144(1):163–97. http://dx.doi.org/10.1016/S0045-7825(96)01165-6.
[15] Nunes C, Soriano H, Filho F. Geometric non-linear analysis of space frame with rotation greater than 90, with euler angles and quasi-fixed local axes system. Int J Non-Lin Mech 2003;38(8):1195–204. http://dx.doi.org/10.1016/S0020-7462(02)00064-1.
[16] Nanakorn P, Vu L. A 2d field-consistent beam element for large displacement analysis using the total lagrangian formulation. Finite Elem Anal Des 2006;42(14):1240–7. http://dx.doi.org/10.1016/j.finel.2006.06.002.
[17] Almeida CA, Albino JC, Menezes IF, Paulino GH. Geometric nonlinear analyses of functionally graded beams using a tailored lagrangian formulation. Mech Res Commun 2011;38(8):553–9. http://dx.doi.org/10.1016/j.mechrescom.2011.07.006.
[18] Battini J-M, Pacoste C. Co-rotational beam elements with warping effects in instability problems. Comp Meth Appl Mech Eng 2002;191(17):1755–89. http://dx.doi.org/10.1016/S0045-7825(01)00352-8.
[19] Felippa C, Haugen B. A unified formulation of small-strain corotational finite elements: I. Theory. Comp Meth Appl Mech Eng 2005;194(21):2285–335. http://dx.doi.org/10.1016/j.cma.2004.07.035.
[20] Urthaler Y, Reddy JN. A corotational finite element formulation for the analysis of planar beams. Commun Numer Meth Eng 2005;21(10):553–70. http://dx.doi.org/10.1002/cnm.773.
[21] Le T-N, Battini J-M, Hjiaj M. A consistent 3d corotational beam element for nonlinear dynamic analysis of flexible structures. Comp Meth Appl Mech Eng 2014;269:538–65. http://dx.doi.org/10.1016/j.cma.2013.11.007.
[22] Pham D, Narayanaswamy S, Qian X, Sobey A, Achintha M, Shenoi A. Composite riser design and development a review. In: Soares CG, Shenoi RA, editors. Analysis and design of marine structures V. CRC Press; 2015. p. 637–45 [Ch. 72].
[23] Salama M, Stjern G, Storhaug T, Spencer B, Echtermeyer A. The first offshore field installation for a composite riser joint. In: Offshore technology conference, 6–9 May, vol. 55. Houston (TX); 2002.
[24] Aslan Z, Daricik F. Effects of multiple delaminations on the compressive, tensile, flexural, and buckling behaviour of e-glass/epoxy composites. Compos Part B: Eng 2016;100:186–96. http://dx.doi.org/10.1016/j.compositesb.2016.06.069.
[25] Koizumi M. Fgm activities in japan. Compos Part B: Eng 1997;28(1):1–4. http://dx.doi.org/10.1016/S1359-8368(96)00016-9.
[26] Meziane MAA, Abdelaziz HH, Tounsi A. An efficient and simple refined theory for buckling and free vibration of exponentially graded sandwich plates under various boundary conditions. J Sandw Struct Mater 2014;16(3):293–318. http://dx.doi.org/10.1177/1099636214526852.
[27] Mahi A, Bedia EAA, Tounsi A. A new hyperbolic shear deformation theory for bending and free vibration analysis of isotropic, functionally graded, sandwich and laminated composite plates. Appl Math Model 2015;39(9):2489–508. http://dx.doi.org/10.1016/j.apm.2014.10.045.
[28] Bourada M, Abdelhakim K, Mohammed Sid Ahmed H, Tounsi A. A new simple shear and normal deformations theory for functionally graded beams. Steel Compos Struct 2015;18(2):409–23. http://dx.doi.org/10.12989/scs.2015.18.2.409.
[29] Bennoun M, Houari MSA, Tounsi A. A novel five-variable refined plate theory for vibration analysis of functionally graded sandwich plates. Mech Adv Mater Struct 2016;23(4):423–31. http://dx.doi.org/10.1080/15376494.2014.984088.
[30] Belabed Z, Houari MSA, Tounsi A, Mahmoud S, Bg OA. An efficient and simple higher order shear and normal deformation theory for functionally graded material (FGM) plates. Compos Part B: Eng 2014;60:274–83. http://dx.doi.org/10.1016/j.compositesb.2013.12.057.
[31] Sofiyev A, Kuruoglu N. Buckling and vibration of shear deformable functionally graded orthotropic cylindrical shells under external pressures. Thin-Wall Struct 2014;78:121–30. http://dx.doi.org/10.1016/j.tws.2014.01.009.
[32] Sofiyev A. Nonlinear free vibration of shear deformable orthotropic functionally graded cylindrical shells. Compos Struct 2016;142:35–44. http://dx.doi.org/10.1016/j.compstruct.2016.01.066.
[33] Sofiyev A. Large amplitude vibration of FGM orthotropic cylindrical shells interacting with the nonlinear winkler elastic foundation. Compos Part B: Eng 2016;98:141–50. http://dx.doi.org/10.1016/j.compositesb.2016.05.018.
[34] Sofiyev A, Hui D, Haciyev V, Erdem H, Yuan G, Schnack E, et al. The nonlinear vibration of orthotropic functionally graded cylindrical shells surrounded by an elastic foundation within first order shear deformation theory. Compos Part B: Eng 2017;116:170–85. http://dx.doi.org/10.1016/j.compositesb.2017.02.006.
[35] Tutuncu N, Ozturk M. Exact solutions for stresses in functionally graded pressure vessels. Compos Part B: Eng 2001;32(8):683–6. http://dx.doi.org/10.1016/S1359-8368(01)00041-5.
[36] Malvern LE. Introduction to the mechanics of a continuous medium. 1st ed. Englewood Cliffs: Prentice-Hall; 1969.
[37] Meirovitch L. Elements of vibration analysis. 2nd ed. New York: McGraw-Hill; 1986.
[38] Timoshenko S, Gere JM. Theory of elastic stability. 2nd ed. Mineola: Dover Publications; 2009.
[39] Lee S-L, Manuel FS. Large deflections and stability of elastic frames. J Eng Mech-ASCE 1968;94:521–48.
[40] Lages E, Paulino G, Menezes I, Silva R. Nonlinear finite element analysis using an object-oriented philosophy – application to beam elements and to the cosserat continuum. Eng Comp 1999;15(1):73–89. http://dx.doi.org/10.1007/s003660050006.
[41] Souza R. Force-based finite element for large displacement inelastic analysis of frames, Ph.D. thesis. University of California; 2000.
[42] Chan SL. Large deflection dynamic analysis of space frames. Comp Struct 1996;58(2):381–7. http://dx.doi.org/10.1016/0045-7949(95)00145-7.
[43] Bathe K, Ramm E, Wilson EL. Finite element formulations for large deformation dynamic analysis. Int J Numer Meth Eng 1975;9(2):353–86. http://dx.doi.org/10.1002/nme.1620090207.
[44] McNamara JF, OBrien PJ, Gilroy SG. Nonlinear analysis of flexible risers using hybrid finite elements. J Offsh Mech Arctic Eng 1988;110(3):197–204. http://dx.doi.org/10.1115/1.3257051.